

## Research Paper

## A general discrete element modelling method and harvest process for wheat plants

Jianhua Fan <sup>a</sup>, Liang Zhang <sup>a</sup>, Kai Sun <sup>b</sup>, Xiaoyan Qian <sup>a</sup>, Lu Wang <sup>a,c,\*</sup>, Jianqun Yu <sup>b</sup><sup>a</sup> School of Mechanical and Aerospace Engineering, Jilin University, Changchun, 130025, China<sup>b</sup> School of Biological and Agricultural Engineering, Jilin University, Changchun, 130022, China<sup>c</sup> College of Food Science and Engineering, Jilin University, Changchun, 130062, China

## ARTICLE INFO

## ABSTRACT

## Keywords:

DEM

Wheat ear model

Wheat stalk model

Cutting and threshing tests

A general modelling approach for mature wheat plants with continuous deformation and breakable characteristics is proposed. First, by analysing the shape and size of three typical wheat plants as well as the coordinates of the discrete particles, the geometrical models of the wheat stalk, ear and grain that compose the wheat plant are constructed. Then, the physical and contact mechanical parameters of the wheat plant are determined and verified via a series of actual tests, including moisture measurement, drainage method, slope test and inclined plane drop test. In addition, the bonding mechanical parameters are obtained by analysing the results of the tensile, compression and shear experiments. On the basis of the above work, the mechanical model of the wheat ear, grain and stalk is constructed considering Hertz-Mindlin contact and bonding models with the discrete element method. Finally, the proposed wheat plant model is validated and verified by comparing the experiment and simulation results in terms of the harvest process including cutting and threshing. The results showed that the cutting force and total threshing rate obtained from the simulations differ from the actual test values by no more than 4.4 % and 9 %, respectively. The strong agreement between the simulation and experimental results indicates the feasibility and reliability of the proposed general modelling method for the wheat plant. In summary, the present study provides an effective tool to analyse the wheat harvest process and agricultural machinery design.

## Nomenclature

(continued)

$A_s$	Stalk cross-sectional area, $\text{m}^2$	$R_{\text{spikelet}}^j$	Radius of the particle in the j-th spike axial segment, m
$D_r$	Diameter of the spike axis of the wheat ear, m	$R_r^i$	Transformation matrix for the coordinates of the i-th spikelet
$D_s$	Diameter of stalk internode, m	$R_x$	Transformation matrix for a rotation of $\alpha$ angle around the x-axis
$e$	Coefficient of restitution	$R_y$	Transformation matrix for a rotation of $\beta$ angle around the y-axis
$E$	Young's modulus, Pa	$T_g$	Thickness of wheat grain, m
$E^*$	Effective Young's modulus, Pa	$T_r^i$	Global coordinate transformation matrix for the i-th spikelet
$F_{\text{contact}}^t$	Tangential contact force, N	$U_d^i$	Threshing rate of the i-th collection box, %
$F_c$	Compression force, N	$U_m^i$	Impurity distribution rate of the i-th collection box, %

$F_{\text{cut}}$	Cutting force, N	$U_o$	Total threshing rate, %
$F_{\text{contact}}^n$	Normal contact force, N	$v_{\text{con}}$	Conveying speed, $\text{m s}^{-1}$
$F_{\text{damp}}^n$	Normal damping force, N	$v_{\text{cut}}$	Cutting speed, $\text{m s}^{-1}$
$F_{\text{damp}}^t$	Tangential damping force, N	$v_n$	Normal relative velocity, $\text{m s}^{-1}$
$F_{\text{max}}^n$	Maximum normal critical force, N	$v_t$	Tangential relative velocity, $\text{m s}^{-1}$
$F_{\text{max}}^t$	Maximum tangential critical stress, N	$W_g$	Width of wheat grain, m
$F_{\text{total}}$	Total contact force between particles, N	$x_r^i$	Initial local x-axis coordinates of the i-th spikelet particle
$G$	Shear modulus, Pa	$X_r^i$	Global x-axis coordinate of the i-th spikelet particle
$G^*$	Effective shear modulus, Pa	$x_{\text{stalk},j}^i$	Local x-axis coordinates of the i-th particle in the j-th stalk internode
$k_a$	Coefficient of axial segment particle radius	$y_r^i$	Initial local y-axis coordinates of the i-th spikelet particle

(continued on next column)

(continued on next page)

\* Corresponding author. School of Mechanical and Aerospace Engineering, Jilin University, Changchun, 130025, China.

E-mail address: [luwang@jlu.edu.cn](mailto:luwang@jlu.edu.cn) (L. Wang).

(continued)

$k_c$	Radius of curvature factor	$y_r^i$	Global y-axis coordinate of the $i$ -th spikelet particle
$k_{damp}^n$	Normal damping coefficient	$y_{stalk,j}^i$	Local y-axis coordinates of the $i$ -th particle in the $j$ -th stalk internode
$k_{damp}^t$	Tangential damping coefficient	$z_r^i$	Initial local z-axis coordinates of the $i$ -th spikelet particle
$K_n$	Normal stiffness, N m <sup>-1</sup>	$Z_r^i$	Global z-axis coordinate of the $i$ -th spikelet particle
$K_t$	Shear stiffness, N m <sup>-1</sup>	$z_{stalk,j}^i$	Local z-axis coordinates of the $i$ -th particle in the $j$ -th stalk internode
$K_{unit}^n$	Normal stiffness per unit area, N m <sup>-3</sup>	$\alpha$	Growth angle of spikelet, °
$K_{unit}^t$	Shear stiffness per unit area, N m <sup>-3</sup>	$\beta$	Outer offset angle of spikelet, °
$l_e$	Effective length, m	$\delta_c$	Shape variable in compression, m
$L_g$	Length of wheat grain, m	$\delta_{contact}^n$	Normal overlap displacement, m
$L_s$	Length of stalk internode, m	$\delta_{contact}^t$	Tangential contact displacement, m
$m_{all}^i$	Total mass in the $i$ -th collection box, kg	$\delta_n$	Normal displacement, m
$m_{box,grain}^i$	Total mass of grains in the collection box, g	$\delta_t$	Tangential displacement, m
$m_{total,grain}^i$	Total mass of grains, kg	$\mu$	Static friction coefficient
$m_{grain}^i$	Mass of grains in the $i$ -th collection box, kg	$\nu$	Poisson's ratio
$m_{mis}^i$	Mass of impurities in the $i$ -th collection box, kg	$\rho_{grain}$	Density of wheat grain, kg m <sup>-3</sup>
$m_s$	Mass of stalk internode, kg	$\rho_{stalk}$	Density of wheat stalk, kg m <sup>-1</sup>
$n$	Rotation speed, rpm	$\sigma_{max}$	Normal critical stress, Pa
$Q$	Feeding mass, kg	$\tau_{max}$	Tangential critical stress, Pa
$R^*$	Effective radius, m		
$R_c$	Radius of small connecting sphere particle, m		Abbreviations
$r_{contact}$	Contact radius, m	DEM	Discrete element method
$R_{sphere}$	Radius of contact spheres, m	PBM	Parallel Bonding Model

## 1. Introduction

Wheat (*Triticum aestivum*) is one of the most widely planted grain crops in the world, and its cultivation has driven much of the development of agricultural mechanisation. The optimisation of wheat harvesting machinery has become a key approach for improving efficiency and reducing labour inputs (Ji et al., 2022). The harvest process involves collisions between the wheat organs and the machinery components. This complex process has contributed to machinery component design and analysis suffering from high manufacturing costs, long cycle times and seasonal dependence (Chen et al., 2022). To optimise the design of wheat harvesting machinery, it is critical to build accurate wheat plant models to study the mechanical behaviour of plants and crop characteristics.

Wheat plants have biomechanical properties that cause large deformations and fracturing during the harvest process. Currently, most wheat plant models commonly used in operational processes of production are simplified (Lenaerts et al., 2014), and usually ignore the dynamic behaviour of the plant organs. Although the traditional models are easy to calculate, they cannot accurately reflect the real flexural and fracture behaviour of wheat plants under external forces, such as wind and mechanical impacts. In addition, existing studies have mostly focused on the optimal design of mechanical equipment when modelling grain harvesting (Chen et al., 2022; He et al., 2018; Li et al., 2023; Wang et al., 2024). Thus, the lack of understanding of the flexible and fracture properties of the wheat plant when designing machinery makes the collisions with the mechanical equipment prone to generate wheat grain damage, which in turn affects the quality and yield of the grains (Ma et al., 2020).

The discrete element method (DEM), as a numerical method to analyse the motion and interaction of particulate matter, is able to

address the bonding and fractural behaviour of plants. Research on DEM for wheat and other cereals has been used for several aspects, including harvesting, storage, transport, processing and quality testing (Horabik & Molenda, 2016; Li et al., 2017; Wang et al., 2022; Zhou et al., 2020, 2021). Schramm et al. (2019) proposed a DEM-based method to calculate the local damping coefficient and Young's modulus of a flexible wheat stalk, and the global damping coefficient and bond damping were measured and validated by the cantilever beam experiments. Zeng and Chen (2019) developed a DEM model using PFC3D to simulate wheat stalk interaction with tillage machinery and soil, effectively reproducing its dynamic behaviour during tillage. Mao et al. (2020) developed a flexible DEM-based stalk model to investigate grain-stalk separation in a combine harvester, accurately capturing stalk bending, tensile properties and grain separation dynamics under varying straw densities. Shi et al. (2023) constructed a DEM-based mechanical model of wheat stems, integrating the Hertz-Mindlin (no-slip) contact model and the bonded particle model to simulate fracture behaviour under different loading conditions. Generally, DEM provides a robust approach to analyse the mechanical behaviours of wheat by accurately capturing particle behaviour, such as friction, collisions and flexibility. However, the aforementioned methods have mainly focus on the wheat stalk model, without developing a comprehensive plant model that incorporates the bonding interactions between the stalk and the wheat ear axis, as well as between the wheat ear axis and the grains.

In the harvesting process, it is essential to consider the entire plant, including the grains, wheat stalks, and wheat ears. Due to their distinct structural characteristics and functional roles throughout the growth stages, these components need to be modelled and parameterised separately within the DEM modelling framework. Sun et al. (2023) proposed a general DEM-based model consisting of wheat stalks and grains. Fan et al. (2024) proposed a multi-sphere modelling method for describing the mechanical behaviour of wheat grains based on the discrete element method, showing a high accuracy of the model when compared with the validation tests. Horabik et al. (2020) calibrated the parameters of a DEM model of wheat grains, providing a theoretical basis for modelling the physical properties of wheat grains in storage and handling. A discrete elemental model capable of accurately reflecting wheat stalks with destructive properties was also developed by Schramm and Tekeste (2022) and Shi et al. (2023). The mechanical behaviours of stalks including fracture, crushing, bending and shearing during tension were numerically and experimentally explored.

Despite extensive research on the fundamental characteristics of wheat plants and the engineering parameters of mechanised harvesting, the geometric complexity, contact characteristics and mechanical properties of wheat plants are often oversimplified, which affects the accuracy of the models in practical applications. Thus, accurately modelling the continuous deformation and fracture behaviour of wheat plants under external forces remains a challenge. Achieving continuous modelling of deformation and fracture behaviour relies on precisely calculating geometric, contact and mechanical bonding parameters, which govern the plant's structure, deformation and fracture characteristics. The calculation and validation of these parameters is crucial for the model, given the differences in geometry, material properties and fracture behaviour across different parts of the wheat plant. Therefore, the present study focuses on addressing the impact of geometric complexity, contact characteristics and mechanical properties on modelling, proposing a general modelling method suitable for flexible wheat plants.

In this article, a DEM-based modelling method for wheat plants with continuous deformation and breakable properties is proposed. To achieve this target, the characteristics of the geometry and size of three typical wheat varieties are measured and analysed in section 2. Then, the particle arrangement method is employed to obtain a geometry model of a wheat sample. In section 3, the contact and bonding mechanical parameters of wheat organs including stalks and ears are determined and verified by various experiments and simulations. After

that, the harvest process consisting of cutting and threshing is used to verify the accuracy of the flexible wheat plant model in section 4 and section 5, respectively. Finally, the conclusion is presented in section 6. This study not only provides a new modelling approach for wheat harvesting operation but also gives strong support for improving wheat harvesting efficiency and promoting agricultural mechanisation.

## 2. Wheat plant discrete element method

To obtain a general model of wheat plants, three representative wheat varieties, namely Longchun No.2 (LC2), Longmai No.35 (LM35) and Xinkehan No.9 (XKH9), from Northeast China are selected for the study, as shown in Fig. 1. Wheat plants are normally collected at maturity to ensure low moisture content and are suitable for mechanised operations. A mature wheat plant is mainly composed of leaves, stalks, ears and grains. Since the leaves of mature wheat plants become wilted with low water content and brittle, they have little impact on the harvest process. Therefore, the effect of wheat leaves is not taken into account for the plant model, and the present study focuses on the model of wheat stalks, ears and grains.

The actual geometry parameters of the wheat plants obtained from previously detailed measurements are not sufficient to comprehensively model wheat plants accurately. Therefore, a DEM is required to improve model generality and accuracy. By combining DEM modelling of geometrical parameters and calibration of mechanical tests, an accurate and reliable wheat plant model could be achieved. Specifically, the obtained plant geometric parameters are used to solve the coordinates of the discrete particles. After that, the mechanical model of the wheat plant including the contact and bonding model between the particles is built, which makes it possible to analyse the behaviour of wheat plants under different collision conditions. To guarantee the model accuracy, it is also necessary to determine the relevant mechanical parameters through a series of tests. These experiments are used to calibrate and validate the mechanical model, ultimately resulting in a model that realistically reflects the continuous deformation and breakable characteristics of the wheat plant.

### 2.1. Geometric parameters measurement and model establishment of wheat stalk

To characterise the structure and geometric properties of wheat stalks, fifty wheat samples of each variety are randomly selected. The

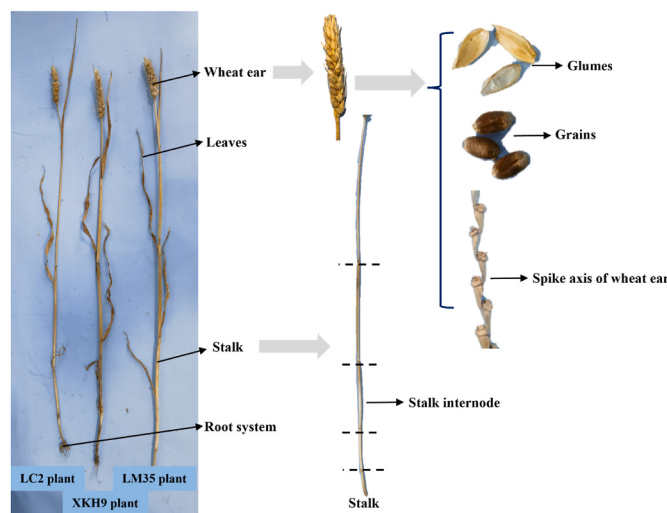


**Fig. 1.** Mature wheat plant for Longchun No.2 (LC2), Longmai No.35 (LM35) and Xinkehan No.9 (XKH9), composing root system, wheat stalk, leaves and wheat ear.

experimental analysis of three wheat varieties indicates that the stalk of the mature wheat plant can be regarded as a slender cylinder. The mean number of internodes for LC2 is  $4.06 \pm 0.2375$ , while the mean number of internodes for LM35 and XKH9 is  $4.92 \pm 0.2713$ . These internodes have different lengths, outer diameters, and masses. The internodes below the wheat ear are sequentially defined as the first to the fifth internode.

The relationship between stalk length, mass, diameter and internode number is investigated, the internode length ( $L_s$ ) decreases with increasing internode number. The first internode is the longest with a length of about 350 mm and the last internode is the shortest with a length of about 50 mm. In addition, the stalk mass of three wheat varieties is presented in Fig. 2b. It is found that the mass of the internodes ( $m_s$ ) varies significantly among the varieties, with a gradual decrease in the mass of the 2nd to 5th internodes. The mass of the 1st internode is marginally less than the 2nd one. Fig. 2c illustrates the external stalk diameter of each internode ( $D_s$ ) gauged with a digital calliper. Wheat stalks exhibit a tendency to have thicker internodes in the middle and thinner internodes at the ends.

After obtaining the geometric parameters, the wheat stalk model can be established using identical internode particles sequentially arranged along the axis. Due to the deformation of wheat stalks, each internode of the wheat stalk is divided into segments connected by 3–6 flexible connection points, depending on the internode length (the longer the stalk, the more flexible connection points are needed). The bonding parameters for these connection points are calculated using the bonded particle model (Guo et al., 2013; Schramm et al., 2019). In this way, the stalk model has realistic conditions for bending and deformation. Then, a flexible wheat stalk is formed in the commercial software EDEM 2018 (DEM Solutions Ltd., Edinburgh, Scotland, UK), where mega-particles are generated and the segments are connected by the bonded particle model, as shown in Fig. 3. The 3–6 flexible connection points at the internodes of the stalk (at the bonding position) can be breakable, while the other parts (the mega-particles) are unbreakable rigid connections. The detail of the bonded particle model is described in section 2.5.

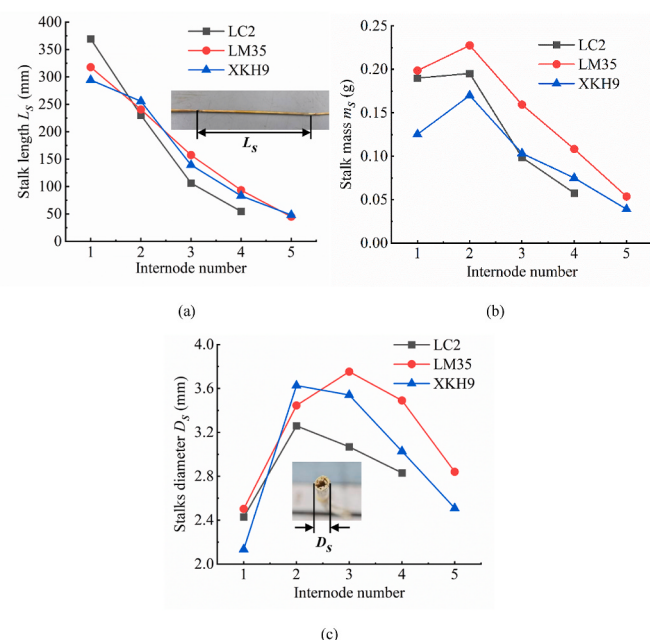


**Fig. 2.** Relationship between geometry parameters of wheat stalks and internode numbers. (a) Stalk length, (b) mass and (c) diameter versus internode number.

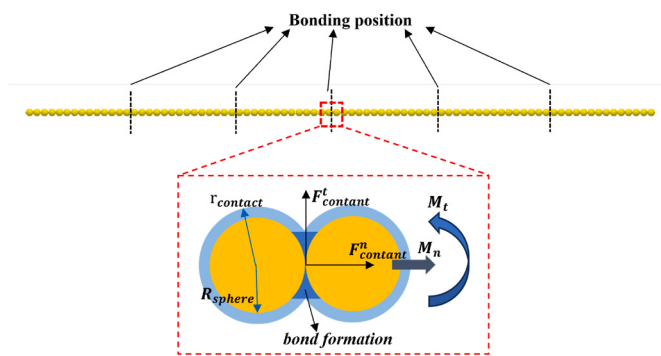


**Fig. 3.** The 2nd internode of LM35 and schematic diagram of the bonded particle model.

## 2.2. Geometric parameters measurement and model establishment of wheat ear

For the three studied wheat varieties, a wheat ear is situated at the top of the plant and connects with the first stalk internode through the spike axis. The wheat ear consists of a spike axis and 10 to 14 spikelets. The spike axis of the wheat ear usually consists of multiple segments that are connected by nodes. Spikelets grow on each node and are staggered on either side of the spike axis. Each spikelet of the selected three varieties is measured to contain 2 to 3 grains, with an average of 2.82. Regarding the grain model, the grain shape can be approximated with a single ellipsoid model (Fan et al., 2024; Sun et al., 2022). An ellipsoid model combining the rigid mega-particle model is employed to describe the actual wheat grain. The more sub-spheres that are used to fill the grain particle, the closer the configuration of the grain model will be to the actual one, resulting in a higher accuracy. However, the number of sub-spheres affects the computational cost. Therefore, to balance the model accuracy and computation efficiency, a 9-sphere mega-particle DEM model is established to describe a wheat grain in this study. The major and minor axes of the ellipsoid represent the length  $L_g$  and the equivalent width  $\frac{W_g + T_g}{2}$  of a wheat grain, where its triaxial dimensions (length  $L_g$ , width  $W_g$  and thickness  $T_g$ ) are listed in Table 1.

The geometric parameters of the wheat ear for three varieties are measured as listed in Table 2. The structure of the glumes has a minimal impact on the overall mechanical properties and behaviour of the wheat plant. Besides, modelling thin-shell structures of glumes using DEM takes a large computational cost. Thus, the physical structure of the glumes is omitted in the wheat plant model for the sake of simplification and improving computational efficiency. Then, the wheat ear model can be built according to the measurement results. It is found that the spike axis of the wheat ear presents an “S” shape as shown in Fig. 4a. To approximate the actual outline, several particles are bonded together to constitute axis segments, whose diameter increases linearly from the bottom to top. The diameter of a particle in the middle part is equal to the measured diameter  $D_r$  and the particle number of each axial segment  $N_0$  is equal to 5 according to the experiment results. The spike axis particles are indirectly connected to the wheat grain particles by small connecting sphere particles with radius  $R_c = 0.5$  mm. The geometrical model of the wheat ear is shown in Fig. 4b. The structure of the glumes has a minimal impact on the overall mechanical properties and behaviour of the wheat plant (Sun et al., 2023). Modelling the thin-shell

**Table 2**  
Geometrical parameters of the wheat ear.

	LC2	LM35	XKH9
Length of wheat ear $L_r$ (mm)	76.70	77.10	90.70
Spikelet number $N_r$	11.90	13.40	12.30
Spikelet spacing $l_n$ (mm)	6.61	6.80	6.30
Diameter of spike axis $D_r$ (mm)	2.12	1.95	2.05
Growth angle $\alpha$ (°)	20.23	21.33	22.50
Outside offset angle $\beta$ (°)	27.70	28.97	34.60

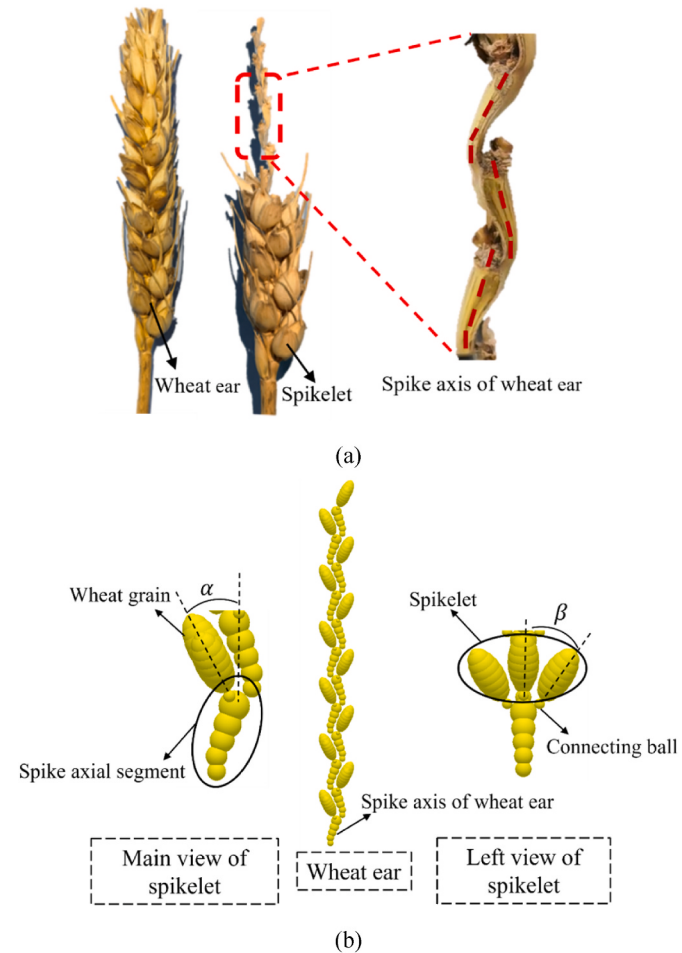


**Fig. 4.** Wheat ear. (a) Example images of the wheat ear, spikelet and spike axis; (b) Geometric model of the wheat ear, grain, spikelet, spike axis segment, growth angle ( $\alpha$ ) and outside offset angle ( $\beta$ ).

structures of glumes using DEM will also have a large computational cost. Thus, the physical structure of the glumes is omitted in the wheat plant model for the sake of simplification and improving computational efficiency.

Based on the plant sample characteristic, each spikelet grows on the axis at a certain angle, which is defined as growth angle  $\alpha$ . Furthermore, the angle between the lateral grain and the middle grain of each spikelet is defined as the outside offset angle  $\beta$  (Fig. 4b). The arrangement of the spikelet on the axis of the wheat ear is uneven because the length of the spike axial segments varies from one variety to another. To facilitate modelling and rationalise the arrangement, a uniform distribution is made with the average spacing of spikelet and the number of grains per spikelet set to 3, since the mean value is 2.82.

To make the model of the wheat plant proposed in this study universal, the relationship between the shape and size of each wheat organ is analysed including the length ( $L_s$ ) and diameter ( $D_s$ ) of the stalk

**Table 1**  
Triaxial dimensions of wheat grains.

	LC2	LM35	XKH9
Length of wheat grain $L_g$ (mm)	6.04	6.07	6.29
Width of wheat grain $W_g$ (mm)	3.16	3.18	2.99
Thickness of wheat grain $T_g$ (mm)	2.74	2.82	2.57

internode, the length of the wheat ear ( $L_r$ ) and the diameter of the spike axis ( $D_r$ ), the length of the wheat ear ( $L_r$ ) and spikelet number ( $N_r$ ), respectively. The results of the polynomial fitting are shown in Table 3. It can be found that there is a strong correlation between  $L_s$  and  $D_s$ ,  $L_r$  and  $D_r$ , and  $L_r$  and  $N_r$ . Thus, the diameter of stalk internode and the diameter of the spike axis, as well as the spikelet number, can be calculated from the length of the stalk internode and length of the wheat ear, which facilitates a generalised model of wheat plants.

### 2.3. Particle coordinate solution for wheat plant model

For the wheat plant model, the local coordinate system of each stalk internode and spike axial segment of the wheat ear is established, which is solved by coordinate translation and rotation transformation. Then, the particle coordinates of the global coordinate system for each organ of the whole wheat plant are obtained by translation transformation. Finally, the wheat plant model is constructed in the commercial software EDEM.

The particles composing each stalk internode are linearly arranged in sequence. Taking the first particle of the stalk internode as the local coordinate origin, the coordinates of the component particles can be given:

$$(x_{stalk,j}^i, y_{stalk,j}^i, z_{stalk,j}^i) = (0 \ 0 \ z_{stalk,j}^{i-1} + 0.9 \cdot D_s^j) \quad (1)$$

where  $x_{stalk,j}^i$ ,  $y_{stalk,j}^i$  and  $z_{stalk,j}^i$  represent the local coordinates of the  $i$ -th particle,  $i = 1, 2, \dots, N_{stalk}^j$ , where  $N_{stalk}^j$  mean the particle number of the  $j$ -th stalk internode.  $D_s^j$  stands for the particle diameter.

Each spike axial segment consists of 5 particles, with the first particle at the bottom of the axial segment being the local coordinate origin, and the radius of the particles in the axial segment linearly increases according to Eq. (2):

$$R_{\text{spikelet}}^j = k_a \cdot \frac{D_r}{2} \quad (2)$$

**Table 3**  
Relationship between wheat stalk and ear parameters.

Variety	Dependent variable	Independent variable	Expression	$R^2$
LC2	$D_s$	$L_s$	$D_s = 6.19 \times 10^{-8} L_s^3 - 6.14 \times 10^{-5} L_s^2 + 0.014 L_s + 2.28$	0.79
	$D_r$	$L_r$	$D_r = -4.05 \times 10^{-8} L_r^3 + 7.30 \times 10^{-5} L_r^2 + 0.012 L_r + 0.77$	0.88
LM35	$N_r$	$L_r$	$N_r = 1.28 \times 10^{-5} L_r^3 - 1.88 \times 10^{-3} L_r^2 + 0.242 L_r - 1.02$	0.91
	$D_s$	$L_s$	$D_s = 2.42 \times 10^{-7} L_s^3 - 1.72 \times 10^{-4} L_s^2 + 0.033 L_s + 1.72$	0.82
	$D_r$	$L_r$	$D_r = -1.24 \times 10^{-5} L_r^3 + 3.21 \times 10^{-3} L_r^2 - 0.255 L_r + 8.026$	0.85
XKH9	$N_r$	$L_r$	$N_r = -1.75 \times 10^{-4} L_r^3 + 4.87 \times 10^{-2} L_r^2 - 4.36 L_r + 138.6$	0.95
	$D_s$	$L_s$	$D_s = 1.01 \times 10^{-7} L_s^3 - 1.07 \times 10^{-4} L_s^2 + 0.027 L_s + 1.49$	0.80
	$D_r$	$L_r$	$D_r = 3.40 \times 10^{-5} L_r^3 + 8.20 \times 10^{-3} L_r^2 + 0.668 L_r - 16.36$	0.83
	$N_r$	$L_r$	$N_r = 3.68 \times 10^{-5} L_r^3 - 7.19 \times 10^{-3} L_r^2 + 0.530 L_r - 2.49$	0.87

where  $R_{\text{spikelet}}^j$  means the radius of the  $j$ -th axial segment particle,  $k_a$  is the coefficient of axial segment particle radius.

A local coordinate system is established to solve for the coordinates of the spikelet particles, the particle centre at the top of the corresponding spike axial segment is the coordinate origin. The position of the grain particles on each spikelet is then determined by coordinate translation and rotation transformation. First, a coordinate rotational transformation is performed on the connected particles and grain particles around the Y-axis to obtain the relative coordinate positions of the three-grain particles in the spikelet. The transformation matrix of the coordinates of the grains on both sides in the  $i$ -th spikelet is given by Eq. (3):

$$R_r^i(\pm\beta) = (x_r^i, y_r^i, z_r^i) \cdot R_y(\pm\beta) \quad (3)$$

where  $x_r^i$ ,  $y_r^i$  and  $z_r^i$  are the initial locations of the  $i$ -th spikelet particle,  $i = 1, 2, \dots, n$ .  $R_y(\beta)$  means the rotation transformation matrix around the Y-axis:

$$R_y(\beta) = \begin{bmatrix} \cos \beta & 0 & -\sin \beta \\ 0 & 1 & 0 \\ \sin \beta & 0 & \cos \beta \end{bmatrix} \quad (4)$$

Then, a coordinate rotation transformation of the grains in the spikelet around the X-axis is performed to obtain the relative coordinate position of the spikelet with respect to the spike axis of the wheat ear. The transformation matrix of the coordinates of the  $i$ -th spikelet is given by Eq. (5):

$$R_r^i(\beta(\pm\alpha)) = \begin{bmatrix} R_i(\beta) \\ R_i \\ R_i(-\beta) \end{bmatrix} \cdot R_x(\pm\alpha) \quad (5)$$

where  $R_x(\alpha)$  is the coordinate rotation transformation matrix around the X-axis:

$$R_x(\alpha) = \begin{bmatrix} 1 & 0 & 0 \\ 0 & \cos \alpha & -\sin \alpha \\ 0 & \sin \alpha & \cos \alpha \end{bmatrix} \quad (6)$$

Finally, the local coordinates of spikelet particles including grain particles and connecting ball particles are transformed into global coordinates according to Eq. (7):

$$(X_r^i, Y_r^i, Z_r^i) = R_r^i(\beta(\pm\alpha)) + T_r^i \quad (7)$$

where  $T_r^i$  is the global coordinate transformation matrix for the  $i$ -th spikelet.

On the above basis, the final geometric model of a wheat plant is obtained as demonstrated in Fig. 5a, whose morphology is consistent with the physical wheat plant (Fig. 5b), except for the omission of the glumes.

### 2.4. DEM contact model

In the discrete element method, the Hertz-Mindlin model is widely employed to simulate the contact behaviour of various particulate materials, such as particle flow, accumulation, transport and fragmentation (Fei et al., 2023; Zhao et al., 2018). The wheat organs are regarded as non-spherical particles, the moment of inertia of non-spherical particles may update in each calculation iteration of the global coordinate system. In order to address the rotational behaviour efficiently, Euler equations in local coordinate systems are commonly used to model and calculate the rotational motion of non-spherical particles (Dong et al., 2024; Zhong et al., 2016). This method can more accurately capture the particle behaviour under complex mechanics, thereby improving the

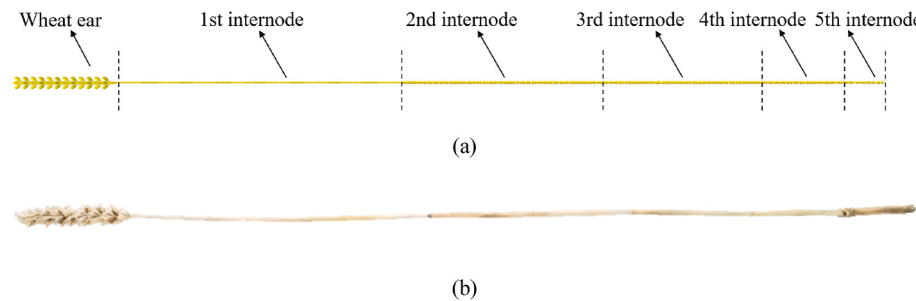


**Fig. 5.** Physical wheat plant and the corresponding model. (a) Geometric model of wheat plant; (b) Physical wheat plant.

accuracy and reliability of simulation results.

The Hertz-Mindlin (no slip) model is a widely used contact model in the DEM, describing the normal and tangential forces between two elastic spherical particles in contact. In this model, the normal force is derived from Hertz contact theory and calculated based on the normal displacement caused by contact deformation (Wang et al., 2020; Zhang et al., 2021). The normal contact force  $\mathbf{F}_{\text{contact}}^n$  is closely related to the effective Young's modulus of the material  $E^*$ , the effective radius  $R^*$ , the normal overlap displacement  $\delta_{\text{contact}}^n$  (Ji et al., 2019) as defined in Eq. (8):

$$\mathbf{F}_{\text{contact}}^n = \frac{4}{3} E^* (R^*)^{\frac{1}{2}} (\delta_{\text{contact}}^n)^{\frac{3}{2}} \quad (8)$$

The effective Young's modulus  $E^*$  is calculated by Eq. (9):

$$\frac{1}{E^*} = \frac{1 - v_1^2}{E_1} + \frac{1 - v_2^2}{E_2} \quad (9)$$

where  $E_1$  and  $E_2$  are the Young's moduli of the two contact spheres,  $v_1$  and  $v_2$  are the Poisson's ratios, respectively. The effective radii  $R^*$  is given as:

$$\frac{1}{R^*} = \frac{1}{R_{\text{sphere}}^1} + \frac{1}{R_{\text{sphere}}^2} \quad (10)$$

where  $R_{\text{sphere}}^1$  and  $R_{\text{sphere}}^2$  are the radii of the two contact spheres, respectively.

Based on Mindlin's contact theory, the tangential contact force  $\mathbf{F}_{\text{contact}}^t$  is related to the tangential stiffness  $K_t$  and the tangential contact displacement  $\delta_{\text{contact}}^t$  (Eq. (11)):

$$\mathbf{F}_{\text{contact}}^t = K_t \delta_{\text{contact}}^t \quad (11)$$

The tangential stiffness  $K_t$  is calculated as:

$$K_t = 8G^* r_{\text{contact}} \quad (12)$$

where  $G^*$  is the effective shear modulus, which incorporates the Young's moduli and Poisson's ratios of the two contacting bodies, defined as:

$$\frac{1}{G^*} = \frac{2(2 - v_1)(1 + v_1)}{E_1} + \frac{2(2 - v_2)(1 + v_2)}{E_2} \quad (13)$$

and  $r_{\text{contact}}$  is the contact radius, defined as:

$$r_{\text{contact}} = (R^* \delta_{\text{contact}}^n)^{\frac{1}{2}} \quad (14)$$

where  $\delta_{\text{contact}}^n$  is the normal overlap displacement.

Damping forces are used to model the energy dissipation process, including normal and tangential damping forces. The normal damping force  $\mathbf{F}_{\text{damp}}^n$  and tangential damping force  $\mathbf{F}_{\text{damp}}^t$  are related to the relative velocities and corresponding damping coefficients, which are given by Eqs. (15) and (16):

$$\mathbf{F}_{\text{damp}}^n = -k_{\text{damp}}^n \mathbf{v}_n \quad (15)$$

$$\mathbf{F}_{\text{damp}}^t = -k_{\text{damp}}^t \mathbf{v}_t \quad (16)$$

where  $k_{\text{damp}}^n$  and  $k_{\text{damp}}^t$  are normal and tangential damping coefficients,  $\mathbf{v}_n$  and  $\mathbf{v}_t$  are normal and tangential relative velocities, respectively.

The total contact force is the sum of the normal and tangential contact forces, along with the respective damping forces, representing the complete interaction between particles (Ji et al., 2019; Zhang et al., 2021), as given by Eq. (17):

$$\mathbf{F}_{\text{total}} = \mathbf{F}_{\text{contact}}^n + \mathbf{F}_{\text{damp}}^n + \mathbf{F}_{\text{contact}}^t + \mathbf{F}_{\text{damp}}^t \quad (17)$$

The translational and rotational motion of particles is then described by Newton's second law:

$$m_i \frac{d\mathbf{v}_i}{dt} = m_i \mathbf{g} + \sum_{j=1}^{n_i} \mathbf{F}_{\text{total}} \quad (18)$$

$$I_i \frac{d\omega_i}{dt} = \sum_{j=1}^{n_i} \mathbf{M} \quad (19)$$

where  $m_i$ ,  $\mathbf{v}_i$  and  $\frac{d\mathbf{v}_i}{dt}$  are the mass, velocity and acceleration of the particle  $i$ .  $n_i$  stands for the total number of particle-particle and particle-wall contacts.  $I_i$ ,  $\omega_i$  and  $\frac{d\omega_i}{dt}$  are the moment of inertia, angular velocity and angular acceleration of the particle  $i$ .  $\mathbf{M}$  is the torque due to the tangential force.

In discrete element calculations, the first step is to determine whether particles are in contact. Based on the calculation model, the total contact force and contact torque are computed. Subsequently, other external forces, such as gravity, are added. Using Newton's second law, the acceleration and angular acceleration of the particles are calculated. Finally, numerical integration is performed to update the position and velocity of the particles.

## 2.5. DEM bonding mechanical model

The Parallel Bonding Model (PBM) achieves mechanical bonding between particles by introducing a "bond" (Potyondy & Cundall, 2004; Sun et al., 2018), as shown in Fig. 3. This bond can withstand both normal and tangential forces, thereby forming a flexible plant structure. The bonded particles that constitute the wheat organs are allowed to displace in both normal and tangential directions, with the continuous accumulation of displacement reflecting the deformation of the stalk. In this model, bond breakage criteria are used to determine whether two adjacent particles remain bonded at the contact area. When the normal stress  $\sigma$  exceeds the critical normal stress  $\sigma_{\text{max}}$  or the tangential stress  $\tau$  exceeds the critical tangential stress  $\tau_{\text{max}}$ , the bonded particles are broken (Schramm et al., 2019; Guo et al., 2013; Zhao et al., 2024; Potyondy et al., 2004). The normal critical stress and the tangential critical stress are given by:

$$\sigma_{\text{max}} \leq \frac{-F_{\text{bond}}^n}{A} + \frac{2M_i}{J} R_{\text{bond}} \quad (20)$$

$$\tau_{max} \leq \frac{-F_{bond}^t}{A} + \frac{2M_n}{J}R_{bond} \quad (21)$$

where  $F_{bond}^n$  and  $F_{bond}^t$  are the normal and tangential bond forces (N),  $M_n$  and  $M_t$  are normal torque and tangential torque (N/m).  $A$ ,  $J$  and  $R_{bond}$  are the contact area ( $\text{m}^2$ ), moment of inertia ( $\text{m}^4$ ) and bond radius (m), respectively. The increments of normal and tangential forces are given by:

$$\delta F_{bond}^n = -\nu_n K_{unit}^{bond,n} A \delta_t \quad (22)$$

$$\delta F_{bond}^t = -\nu_t K_{unit}^{bond,t} A \delta_t \quad (23)$$

where  $K_{unit}^{bond,n}$  and  $K_{unit}^{bond,t}$  denote the normal and tangential stiffness per unit area ( $\text{N m}^{-3}$ ),  $\delta_t$  is the time step (s). Similarly, the increments of normal and tangential torques are expressed as:

$$\delta M_n = -\omega_n K_{unit}^{bond,t} J \delta_t \quad (24)$$

$$\delta M_t = -\omega_t K_{unit}^{bond,n} \frac{J}{2} \delta_t \quad (25)$$

where  $\omega_n$  and  $\omega_t$  correspond to the normal and tangential angular velocities of the relative motion between particles ( $\text{rad s}^{-1}$ ).

The interactions between particles are controlled by the contact forces of the Hertz-Mindlin (no slip) model. To accurately simulate the bonding behaviour between particles, the model parameters need to be selected and verified appropriately. In Section 3.3, the bonding parameters are calculated and validated through the tests and simulations, with a particular focus on verifying the accuracy of tensile and shear forces to ensure that the bond behaviour at the flexible fibre joints is faithfully represented. This calibration process guarantees that the bonding characteristics are consistent with the anticipated fracture behaviour of the plant structure.

### 3. Materials and methods

#### 3.1. Intrinsic parameters of wheat plants

To conduct the DEM simulations of the wheat plant, the actual moisture content of the wheat organ is measured as an initial step for the test. Five-gram samples of grains or stalks are taken at a time and sliced with a slicer to facilitate faster steam drying. Then, as shown in Fig. 6a, the samples are placed in a moisture meter (DHS-10A, China) to dry until the value of the device's moisture content no longer varied. Five groups of tests are repeated for each variety and each internode.

The mass  $m_g$  and volume  $V_g$  of wheat grains are measured using the drainage method as shown in Fig. 6b. Then, the density  $\rho_{grain}$  of wheat

grains is calculated based on the density definition. Again, five sets of trials are repeated for each variety.

Poisson's ratio of wheat plants is not easy to obtain due to the irregular shape of various parts of wheat plants. Here, Poisson's ratio for wheat stalk and wheat grain is selected as 0.25 (Schramm & Tekeste, 2022) and 0.40 (Moya et al., 2022) according to the previous reports.

#### 3.2. Measurement and verification of contact parameters

To ensure the accuracy of the proposed wheat plant model and perform the corresponding DEM simulations, accurate contact parameters are essential for each organ of the wheat plant, including the static friction coefficient, restitution coefficient and rolling friction coefficient. Consequently, the mechanical behaviour of the wheat plant during the harvesting process is studied.

The coefficients of static friction between grains, stalks and contact materials are measured using an inclined slope test (see Fig. 7a). The test procedure is as follows: First, the grains and stalks are densely spread and adhered to a flat panel to minimise the effects of mechanical interlocking, ensuring that the two materials to be tested are in face-to-face contact. Then, a hydraulic rod is used to gradually increase the angle of the inclined plane. The coefficient of static friction between two materials is determined by the angular value of the ramp. Each group of trials is repeated five times.

The coefficient of restitution is defined as the ratio of the speed before and after the collision, indicating the recovery ability of materials. The coefficient of restitution between wheat organs and contact materials is conducted using the inclined drop test method (Wang et al., 2015), as shown in Fig. 7b. The wheat grains or stalks are released freely from rest and fall onto an inclined surface at an angle of 45° to the ground for collision. The velocity before and after the collision is processed by a high-speed camera. Each test is repeated five times between two materials. The inclined plane drop test method accounts for the effects of different impact and rebound angles, ensuring that the results fall within an acceptable margin of error. Additionally, the post-collision velocities are calculated using velocity vectors in three-dimensional space, which inherently consider the potential influence of the irregular shapes of the grains and stalks on the velocity components.

Wheat grains and stalks are challenging to roll on an inclined surface because of their irregular shapes. Furthermore, the light weight of the stalk made it susceptible to static electricity when rolling. As a result, rolling friction coefficients of grains and stalks based on the principle of energy conservation are not easily accurately determined. Since the measurement process of the rolling friction coefficient is complicated and the error caused by it has little influence on the contact parameters, according to the published references (Liu et al., 2018; Sun et al., 2023), the rolling friction coefficient of grain-grain and grain-wall is set at 0.02,

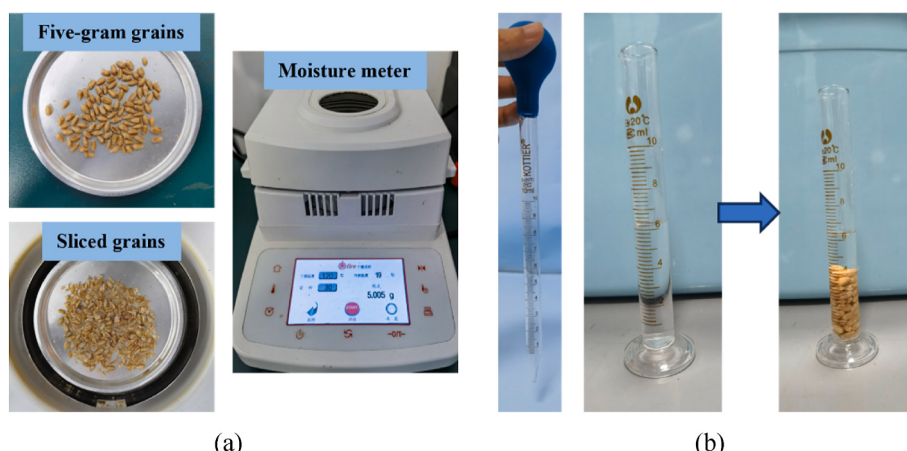


**Fig. 6.** Measuring instruments for wheat plant intrinsic parameters. (a) Moisture measurement; (b) Grain density test using the drainage method.

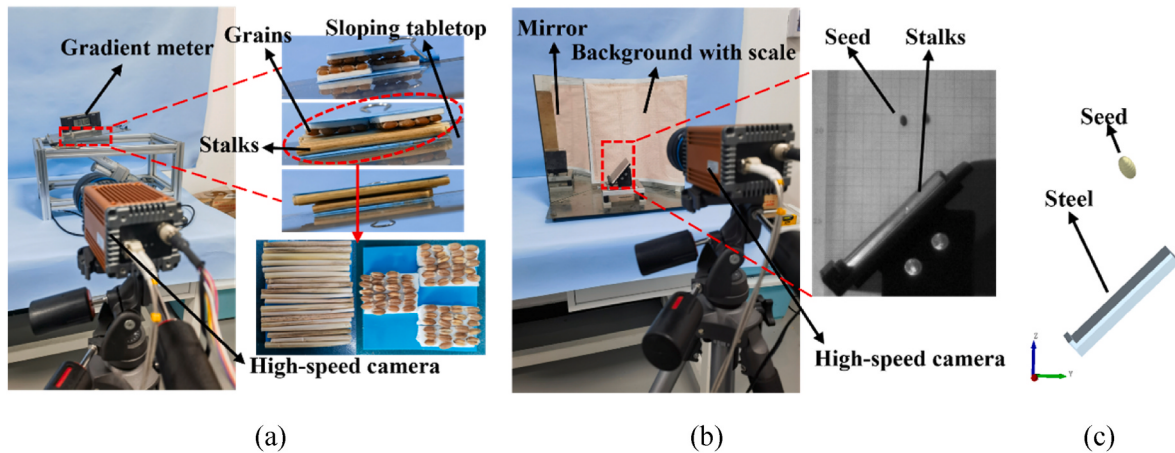


**Fig. 7.** Contact parameter tests and simulations. (a) Slope test; (b) Inclined plane drop test; (c) Inclined plane drop simulation.

while the value for stalk-stalk and stalk-wall is selected as 0.01.

After measuring the contact parameters, verification tests are performed to determine the accuracy of the measured contact parameters. The same working conditions as the inclined plane drop test are set up in the simulations, as shown in Fig. 7c. Then the corresponding static friction coefficient, coefficient of restitution and rolling friction coefficient are input into the established models of wheat grains and stalks. In the simulation validation results of the three varieties, the restitution coefficients of both grains and stalks are generally close to the actual experimental values. The maximum error occurs in the grain-steel contact parameter of LM35, where the simulated value is 0.603, showing a maximum deviation of 5.9 % from the experiment result. Therefore, the contact parameters of grains and stalks can be used for subsequent simulations.

### 3.3. Measurement and verification of bonding parameters

#### 3.3.1. Measurement of mechanical parameters of wheat grains

The mechanical parameters of the wheat grain are measured using a texture meter as shown in Fig. 8. The wheat grain is compressed by placing the wheat grain with the grooved side facing downwards, the force and displacement during compression are measured by the mass tester. Young's modulus  $E$  can be calculated based on the parallel plate compression model. Five replicated trials are done for each variety. The Young's modulus  $E_{grain}$  of the grain is obtained from the following

equation:

$$E_{grain} = \frac{0.338F_c(1 - \nu^2)}{\delta_c^{\frac{3}{2}}} \left[ k_c^U \left( \frac{1}{R_c^U} + \frac{1}{R_c^U} \right)^{\frac{1}{3}} + k_c^L \left( \frac{1}{R_c^L} + \frac{1}{R_c^L} \right)^{\frac{1}{3}} \right] \quad (26)$$

where  $F_c$  is the compression force,  $\delta_c$  is the shape variable in compression,  $\nu$  represents the Poisson's ratio,  $R_c^U$ ,  $R_c^U$ ,  $R_c^L$  and  $R_c^L$  are the principal radii of curvature of the grain compression contact points,  $k_c^U$  and  $k_c^L$  means the coefficients of curvature radius.

#### 3.3.2. Normal mechanical parameters of wheat stalks

The stalk samples are clamped on the fixture of the texture meter and the tensile test is conducted with a tensile speed of  $10 \text{ mm min}^{-1}$ , as presented in Fig. 9a. The force and deformation curves of the stalks during stretching are measured by the texture meter, while the effective length and diameter of the stretched stalks are recorded. Each experiment is repeated five times for each variety. The normal stiffness  $K_n^{stalk}$  of the stalk is determined by the change in force divided by the variation in displacement. The stalks normal stiffness per unit area is calculated by the formula  $K_{unit}^{n,stalk} = \frac{K_n^{stalk}}{A_s}$ , where  $A_s$  is the stalk cross-sectional area. In addition, Young's modulus of the stalks is calculated by the formula  $E_{stalk} = \frac{K_n^{stalk} l_e}{A_s}$ , where  $l_e$  is the effective length. In the tensile test, when the tensile force is greater than the maximum tensile force  $F_{max}^{n,stalk}$ , the stalk would be broken. Thus, the maximum normal critical stress can be calculated:

$$\sigma_{max}^{stalk} = \frac{F_{max}^{n,stalk}}{A_s} \quad (27)$$

#### 3.3.3. Tangential mechanical parameters of stalks

The stalk samples are clamped to the shear fixture of the mass spectrometer as shown in Fig. 10a. The knife cuts vertically downwards at  $10 \text{ mm min}^{-1}$ , then the shear and displacement profiles of the stalks are measured by a texture meter. Each experiment is repeated five times for each variety. During the shearing test, the shear force causes the round cross-section of the stalk to gradually become oval, the upper and lower walls of the stalk are gradually cut off. When the cutting knife cuts to the lower wall of the stalk, the shear force gradually increases until the stalk is completely broken and the shear force reaches the maximum value  $F_{max}^{t,stalk}$ . Therefore, the tangential critical stress of the stalk can be calculated:

$$\tau_{max}^{stalk} = \frac{F_{max}^{t,stalk}}{A_s} \quad (28)$$

In addition, the shear modulus  $G_{stalk}$  of the stalk is calculated from

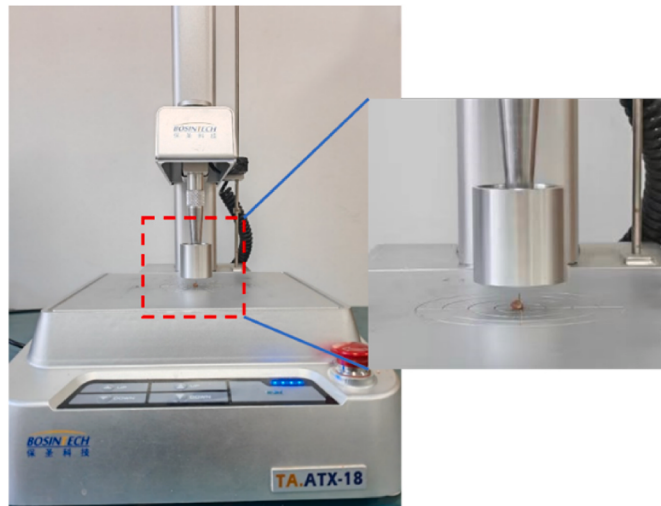


**Fig. 8.** Wheat grain compression test.

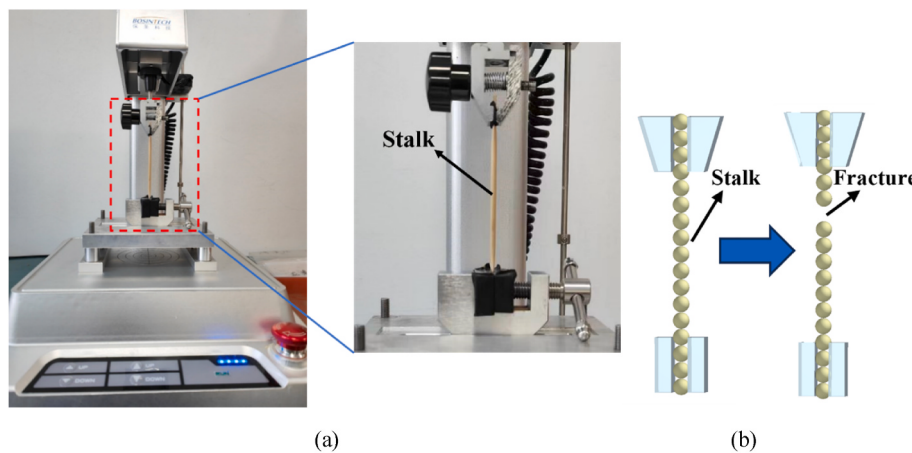


**Fig. 9.** Stalk tensile test and simulation. (a) Stalk tensile test; (b) Stalk tensile simulation.

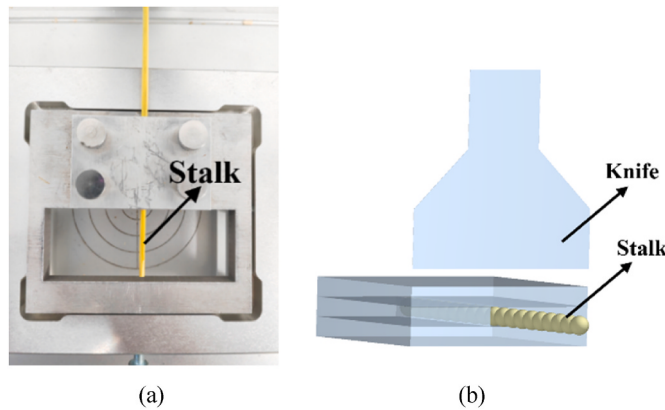


**Fig. 10.** Shear test and tangential critical stress of the stalk internodes. (a) Shear test and (b) corresponding simulation.

Young's modulus  $E_{stalk}$  of the stalk and Poisson's ratio  $\nu$ , which is given:

$$G_{stalk} = \frac{E_{stalk}}{2(1 + \nu)} \quad (29)$$

The shear stiffness per unit area  $K_{unit}^{t,stalk}$  is related to the normal stiffness per unit area  $K_{unit}^{n,stalk}$  and the Poisson's ratio  $\nu$ , which is calculated as:

$$K_{unit}^{t,stalk} = \frac{K_{unit}^{n,stalk}}{2(1 + \nu)} \quad (30)$$

Then, all the calculated mechanical parameters of wheat stalks are listed in **Table 4**.

### 3.3.4. Measurement of mechanical parameters between the spike axis and wheat grain

Tensile and shear tests are conducted at the joint between the spike axis of the wheat ear and the grain. Five sets of repeatable sample tests are conducted for each wheat variety. To prepare the wheat ear samples for tensile and shear tests, all other grains are removed from the spike axis, leaving only a single grain attached. For the tensile test, the lower clamp of the texture meter is used to grip the spike axis, while the upper clamp holds the grain. The sample is stretched at a speed of 10 mm/min, as shown in **Fig. 11a**. For the shear test, the texture meter's clamp secures the spike axis, while a cutting blade moves vertically downward at a speed of 10 mm/min to shear the connection between the grain and the spike axis, as shown in **Fig. 11b**. The mechanical parameters at the joint including Young's modulus  $E_{ear}$ , normal stiffness per unit area  $K_{unit}^{n,ear}$ , normal critical stress  $\sigma_{max}^{ear}$ , tangential critical stress  $\tau_{max}^{ear}$ , shear modulus

**Table 4**  
Measurements of mechanical parameters of wheat stalks.

	No.1	No.2	No.3	No.4	No.5
$E_{stalk}$ (MPa)	LC2 LM35 XKH9	1337.66 1605.05 2340.91	1747.13 1548.52 1251.99	1198.72 1012.52 855.94	716.95 877.59 624.23
$K_{unit}^{n,stalk}$ ( $\times 10^9$ N m $^{-3}$ )	LC2 LM35 XKH9	16.72 20.06 29.26	21.84 19.36 15.65	23.97 20.25 17.12	23.90 29.25 20.81
$\sigma_{max}^{stalk}$ (MPa)	LC2 LM35 XKH9	1.68 2.28 1.90	1.97 1.63 1.12	2.08 1.82 0.80	2.10 1.95 1.03
$G_{stalk}$ (MPa)	LC2 LM35 XKH9	543.76 652.46 951.59	873.57 774.26 626.00	599.36 506.26 427.97	358.48 438.80 312.12
$K_{unit}^{t,stalk}$ ( $\times 10^9$ N m $^{-3}$ )	LC2 LM35 XKH9	6.80 8.16 11.89	10.92 9.68 7.82	11.99 10.13 8.56	11.95 14.63 10.40
$\tau_{max}^{stalk}$ (MPa)	LC2 LM35 XKH9	0.41 0.45 0.20	0.21 0.16 0.11	0.28 0.21 0.14	0.52 0.29 0.19
	None 438.20 431.32				
	None 29.21 28.75				
	None 2.16 2.00				
	None 219.10 215.66				
	None 14.61 14.38				
	None 0.45 0.33				

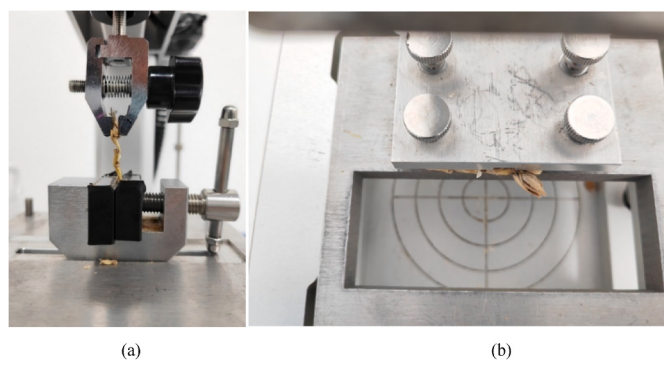


**Fig. 11.** Tensile and shear tests at the joint between the spike axis of wheat ear and grain. (a) Tensile test; (b) Shear test.

$G_{ear}$  and the shear stiffness per unit area  $K_{unit}^{t,ear}$  are calculated in the same way as the stalk, which are listed in **Table 5**. All the mechanical parameters are obtained by conducting the tests five times for each variety.

To determine the accuracy of the measured parameters, the corresponding simulations are carried out to compare the bonding mechanics parameters of wheat stalks and ears. First, the same working conditions

**Table 5**

Measurements of mechanical parameters at the joint between the spike axis of wheat ear and grain.

	LC2	LM35	XKH9
Young's modulus $E_{ear}$ (MPa)	8.41	7.57	6.69
Normal stiffness per unit area $K_{unit}^{n,ear}$ ( $\times 10^9$ N m $^{-3}$ )	0.75	0.81	0.72
Normal critical stress $\sigma_{max}^{ear}$ (MPa)	0.27	0.30	0.28
Shear modulus $G_{ear}$ (MPa)	3.36	3.03	2.68
Shear stiffness per unit area $K_{unit}^{t,ear}$ ( $\times 10^9$ N m $^{-3}$ )	0.30	0.32	0.29
Tangential critical stress $\tau_{max}^{ear}$ (MPa)	0.20	0.21	0.20

are set as in the tensile and shear tests, as presented in Figs. 9b and 10b. Then, the measured parameters are inputted to the established wheat stalk model. The verification process for wheat ears is performed. The results indicate that the maximum tensile force and shear force at each internode of the stalks and wheat ears are close to the actual test values, where the maximum tensile force between each internode of stalks and wheat ears appears in the 1st internode of the stalks of XKH9 with a maximum error of 2.7 %, and the maximum error of 8.8 % in shear force appears in the 2nd internode of the stalks of LM35. Therefore, the bonding parameters of the wheat ears and the individual internodes of the stalks are verified.

#### 3.4. Physical experiment and simulation analysis

The feasibility and accuracy of the proposed wheat ear and stalk modelling method are verified by carrying out physical experiments and related simulations. Cutting and threshing tests are conducted respectively to characterise the harvesting behaviour of wheat plants, providing data and a model basis for the optimal design of the harvesting machinery.

##### 3.4.1. Cutting test and simulation of the wheat plant

In the cutting test, since the stalks are in full contact with the cutting tool, the modelling accuracy of the plant model can be comprehensively verified by simulating this process. In addition, the behaviour during the bonding process can be characterised by analysing the influence of the contact parameters on the dynamic fracture of the stalk. Cutting is the first step during the harvest process. Once the wheat stalks at maturity are cut, the whole plant (partial stalks, ears and grains) enter the conveying system for subsequent threshing. The cutting system is generally a reciprocating cutter, consisting of moving and fixed knives, as shown in Fig. 12. The wheat plant cutting is achieved by the relative motion of two knives, whose relative speed determines the cutting performance. To avoid uncut wheat stalks or the clogging of the cutting system, an efficient relative cutting speed is required.

To analyse the state of motion of the cutter and the cutting of the wheat stalks, a single-factor test is conducted using a completed cutting system to investigate the link between cutting force and cutting speed. The setup for the cutting test is as follows: the cutting height between the

moving knife and the bottom of the fixture is set at 200 mm. The conveying speed of the fixed wheat plant  $v_{con} = 0.4$  m s $^{-1}$ , five cutting speeds  $v_{cut}$  are selected ( $v_{cut} = 0.6, 0.8, 1.0, 1.2$  and  $1.4$  m s $^{-1}$ ) for the cutting tests. The test results are obtained by the multi-channel data sensor on the PC. A high-speed video camera is used to record the time during the cutting test to observe wheat stalk breakage and distribution.

The cutting process of wheat plants is simulated and analysed using the discrete element software EDEM. The simulation setup is consistent with that of the actual test. The cutting simulation steps are as follows: First, the geometry models of the fixed knife, moving knife and plant fixture in the cutting system are imported into EDEM, where the cutting height is set to 200 mm. The cutting height is precisely near the position where cohesive bonds exist in the wheat stalk, which ensures that the particle interactions and bonding behaviour in the simulation closely resemble the actual conditions. The cutting speed of the moving knife is set as a reciprocating linear motion, and the moving knife speed is 1 m s $^{-1}$  at 4 Hz. The conveying speed is 0.4 m s $^{-1}$  and the moving direction is the same as the actual test. The particle factory size is slightly larger than the wheat plant to ensure that the fixture can clamp the wheat plant. Finally, the X-direction cutting force of the plant can be obtained from the post-processing software.

##### 3.4.2. Threshing test and simulation of the wheat plant

In the threshing test, the complex interaction between the wheat plant and the threshing machinery affects the dynamic separation characteristics of the grain and stalk. Moreover, the threshing test can comprehensively verify the adhesive mechanical properties of the plant model by applying friction loads to deform and fracture the wheat plant. Thus, it is feasible to analyse the threshing, crushing and attitude changes of wheat plants at different stages via the simulations, and the main mechanisms of grain loss and impurity content of stripped items under various working conditions can be revealed.

A wheat thresher is used as shown in Fig. 13a, which mainly consists of a speed control motor, drum, sieve plate, collection box, entrance and exit. The test procedure is as follows: the motor is launched to control the drum to rotate at a certain speed, then a certain mass of wheat plants is fed to the entrance of the thresher. The drum and sieve plate rub the wheat ears, causing the grains to drop from the ears into the collection box below, which is numbered 1 through 5 from the exit to the entrance, accordingly. To investigate the effects of drum rotational speeds and feeding amounts on threshing performance, a range of wheat feeding mass  $Q$  (200 g, 250 g, and 300 g) and drum rotational speeds  $n$  (666 rpm, 888 rpm, and 1110 rpm) are selected as the varying factors for the threshing test.

To verify the applicability of the established wheat plant model and the accuracy of the simulation results, an in-depth DEM simulation of the threshing process is performed (implemented in Fig. 13b). Since EDEM features a built-in dynamics module capable of simulating drum rotation and conveyor transport by considering the force applied to the wheat plant, only DEM simulations are employed in the present study

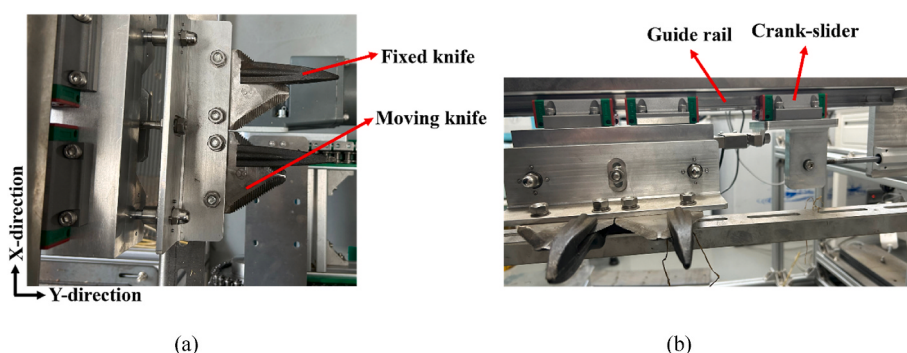
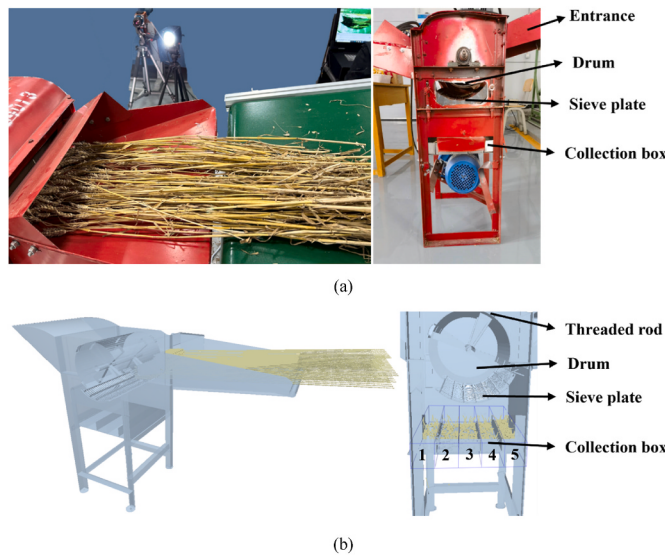


Fig. 12. Images of the cutting system: (a) fixed knife and moving knife; (b) guide rail crank–slider.



**Fig. 13.** Wheat thresher and corresponding simulation model (two views). (a) Wheat thresher; (b) Simulation model of wheat threshing machine. The wheat plants are fed into the thresher from the entrance. The drum and sieve plate rub the ears, causing the grains to fall into the collection boxes below, which are numbered 1 to 5 sequentially from the exit to the entrance.

without implementing two-way coupling with specialising multibody dynamics. In addition, a simplified simulation workflow can be achieved without compromising overall accuracy by minimising the impact of particle interactions on the dynamic response of the drum. Furthermore, the motion of mechanical components, such as the rotating drum, may generate air disturbances. However, physical experiments have shown that these disturbances in the threshing process are very limited compared with other forces, such as impact, friction and compression. Therefore, the effects of airflow on the threshing process are ignored in the DEM simulations. During the simulation process, the wheat plants consistent with the experiment samples are generated in the EDEM software and transported inside the thresher through a conveyor belt. The drum is given the same rotation speed as in the experiment. The wheat grains are kneaded out of the drum and the sieve plate, falling into the collection box. Subsequently, the quality of the grains in the collection box is counted and the threshing rate is calculated.

Three metrics are used to judge the error between the threshing simulation and the actual test. The total threshing rate  $U_o$  is defined as the ratio of the grain mass in the collection box  $m_{\text{grain}}^{\text{box}}$  to the total mass  $m_{\text{grain}}^{\text{total}}$ :

$$U_o = \frac{m_{\text{grain}}^{\text{box}}}{m_{\text{grain}}^{\text{total}}} \quad (31)$$

The second metric is the threshing rate  $U_d^i$  of the  $i$ -th collection box, which is calculated as:

$$U_d^i = \frac{m_{\text{grain}}^i}{m_{\text{grain}}^{\text{total}}} \quad (32)$$

where  $m_{\text{grain}}^i$  is the grain mass in the  $i$ -th collection box.

The third metric is the impurity distribution rate  $U_m^i$  of the  $i$ -th collection box, which is defined as:

$$U_m^i = \frac{m_{\text{mis}}^i}{m_{\text{all}}^i} \quad (33)$$

where  $m_{\text{mis}}^i$  represents the impurity mass, which includes all materials other than wheat grains, in the  $i$ -th collection box.  $m_{\text{all}}^i$  is the total mass

in the  $i$ -th collection box.

## 4. Results and discussion

### 4.1. Parameters of wheat plant

The moisture content test values are presented in Fig. 14a. Wheat grain has an average moisture content of 7.3 %–7.7 %, while the average water content of the stalk internode is 6 %–7 %. The results indicate that the wheat plant samples collected in this paper have low water content, which is suitable for mechanised harvesting operations.

The density measurement results are shown in Fig. 14b, the range of grain density for each variety is between  $1.2 \text{ g cm}^{-3}$  and  $1.4 \text{ g cm}^{-3}$ . Since a solid modelling method is used for the stalk model, which is different from the hollow structure of the actual stalk, the stalk density is represented by linear density to facilitate the alignment of model parameters with actual parameters. It is noted that there is a linear relationship between the density of stalk internodes  $\rho_{\text{stalk}}$  with the internode number as displayed in Fig. 14b. The density per stalk internode ranges from  $0.4 \text{ g m}^{-1}$  to  $1.2 \text{ g m}^{-1}$ , with a gradual increase from the first to the fifth internode. Individual variety XKH9 has slightly less linear density in the fifth internode than in the fourth internode.

The coefficients of static friction between these materials are listed in Table 6. The coefficient of static friction of  $\mu_{\text{grain-stalk}}$  and  $\mu_{\text{grain-belt}}$  are 0.25 and 0.7. The coefficient of static friction  $\mu_{\text{grain-steel}}$ ,  $\mu_{\text{grain-acrylic}}$ ,  $\mu_{\text{stalk-steel}}$ ,  $\mu_{\text{grain-grain}}$  and  $\mu_{\text{stalk-stalk}}$  are little difference, being around 0.4.

The measured coefficients of restitution are shown in Table 6. The coefficients of restitution between grains and grains as well as stalks and belts are the smallest at around 0.4. This coefficient for grains and stalks is the largest at around 0.6. The coefficients of restitution between grain-steel, grain-acrylic (loanword), grain-belt, grain-steel and stalk-stalk are around 0.55.

The average values of Young's modulus  $E_{\text{grain}}$  of the grains, with reference to the parallel plate compression model (Peter and Alan, 1969), are computed and displayed in Fig. 15. For three varieties, the grains' Young's modulus ranges from 160 MPa to 189 MPa.

The Young's modulus of each stalk internode  $E_{\text{stalk}}$  is presented in Fig. 16a. The results show that there is a tendency for Young's modulus to decrease gradually with increasing internode number of the stalks. Young's modulus is the largest in the 1st internode at about 2000 MPa and the smallest in the 5th internode at about 500 MPa. The normal stiffness per unit area of the stalks  $K_{\text{unit}}^{\text{stalk}}$  is shown in Fig. 16b, the results indicate that the normal stiffness of the stalks ranges from  $15 \times 10^9$ – $30 \times 10^9 \text{ N m}^{-3}$ . The normal stiffness per unit area tends to increase gradually with the increase of the internode number. Fig. 16c displays the normal critical stress of the wheat stalk  $\sigma_{\text{max}}^{\text{stalk}}$  in the range of 0.8 and 2.3 MPa. On the whole, except for the 1st internode, the stalk normal critical stress of LC2, LM35 and XKH9 decrease successively.

The tangential critical stress of the stalks calculated with Eq. (28) is

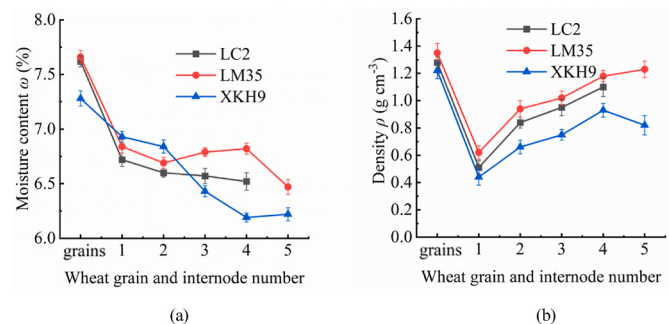


**Fig. 14.** Intrinsic parameters of the wheat plant. (a) Mean moisture content of wheat grains and stalks with standard deviation; (b) Mean density of wheat grains ( $\text{g cm}^{-3}$ ) and stalks ( $\text{g m}^{-1}$ ) with standard deviation.

**Table 6**  
Contact parameters of the wheat plant for three varieties.

	Static friction coefficient $\mu$			Coefficient of restitution $e$		
	LC2	LM35	XKH9	LC2	LM35	XKH9
Grain - steel	0.43	0.51	0.52	0.57	0.51	0.55
Grain - acrylic	0.43	0.38	0.42	0.60	0.57	0.55
Grain - belt	0.63	0.76	0.68	0.56	0.46	0.51
Stalk - steel	0.35	0.33	0.35	0.46	0.57	0.50
Grain - stalk	0.19	0.24	0.27	0.63	0.62	0.62
Stalk - belt	0.73	0.86	0.78	0.43	0.42	0.41
Grain-grain	0.53	0.41	0.54	0.38	0.42	0.48
Stalk-stalk	0.41	0.30	0.36	0.57	0.49	0.48

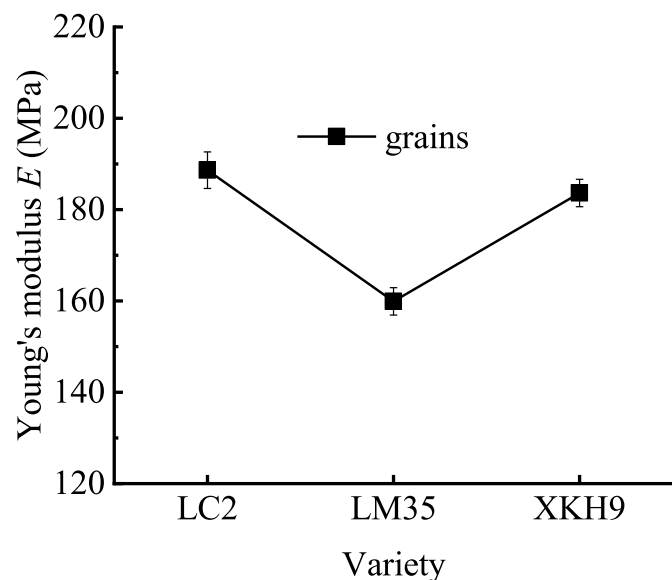


Fig. 15. The mean value of Young's modulus of grains for three wheat varieties.

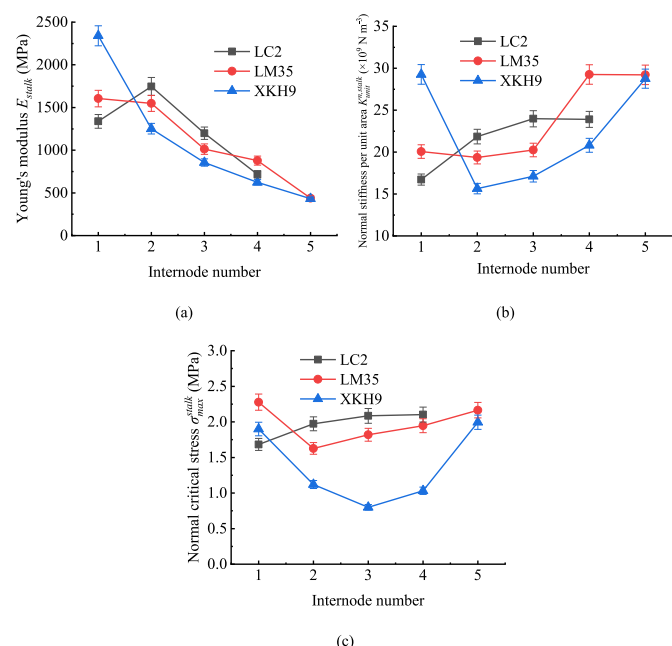


Fig. 16. Mean of measurements of mechanical parameters for the stalk internodes. (a) Young's modulus; (b) Shear stiffness per unit area; (c) Normal critical stiffness.

displayed in Fig. 17. The results show that the values of  $\tau_{max}^{stalk}$  for each variety are between 0.1 and 0.5 MPa. Except for the first internode, there is a tendency for the tangential critical stress of the remaining internodes to increase with the internode number. Overall, the tangential critical stress of LC2, LM35, and XKH9 stalks decreases in that order.

#### 4.2. Analysis of the cutting test and simulation results

Fig. 18 displays the wheat plant cutting results obtained by a single-factor test, showing the relationship between the cutting force  $F_{cut}$  and the cutting velocity. The results reveal that the magnitude of the cutting force decreased with the cutting speed of the moving knife. Here LM35 is used as an example, and as the cutting speed increased from 0.6 to 1.4 m s<sup>-1</sup>, the cutting force of LM35 in the X-direction decreased in the range of 12–19 N. Due to the rapid motion of the moving knife, the chances of the wheat plant being cut at the position of the cutter top are reduced. The cutting force was related to the cutting position of the wheat plant. The cutting force increased gradually from the end of the moving knife to the top. Therefore, an increase in cutting speed resulted in the plant being cut more at the end of the knife, which in turn reduced the cutting force.

Fig. 19a shows the cutting test process of the wheat plant. The red zone indicates the cutting zone, where all four stalks have been severed. When the cutting speed was >1.2 m s<sup>-1</sup>, and it was difficult for all four stalks to be cut off by the cutting knife at the same position. However, the fracture mode of wheat plants changed from cutting to tearing. Fig. 19b presents the simulation of the wheat plant-cutting process. Once the wheat plants had been generated by the particle factory, the fixture with the wheat samples advanced at a conveyor speed of 0.4 m s<sup>-1</sup>. Two groups of wheat samples were cut during the simulation, each group included 4 wheat plants. All the wheat plants were broken at the stalks (see the red zone in Fig. 19b) with a total of two cuts (the main cutting area is in the red zone). The first cut mainly consisted of 2 stalks cut off at the end of the knife, while the remaining 2 stalks were broken at the head of the knife. For the second cut, all the 4 stalks were broken.

During the cutting process, the variation of the cutting force  $F_{cut}$  with time is shown in Fig. 20. There are two peaks that occur for the  $F_{cut}$  corresponding to the two times of cutting wheat samples. The values of the cutting force obtained from the simulations were 10.89 N and 15.56 N, while the average value of the actual test was 14.9 ± 1.9 N. The error between the first cutting force and the actual test was 26.9 %, and the second one was 4.4 %, within the standard deviation of the experimental results. Note that the peak cutting force of the first cut was lower than

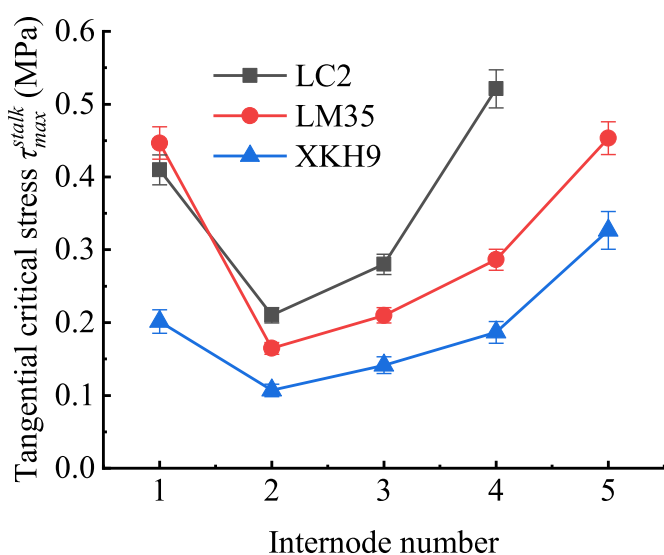


Fig. 17. Tangential critical stress.

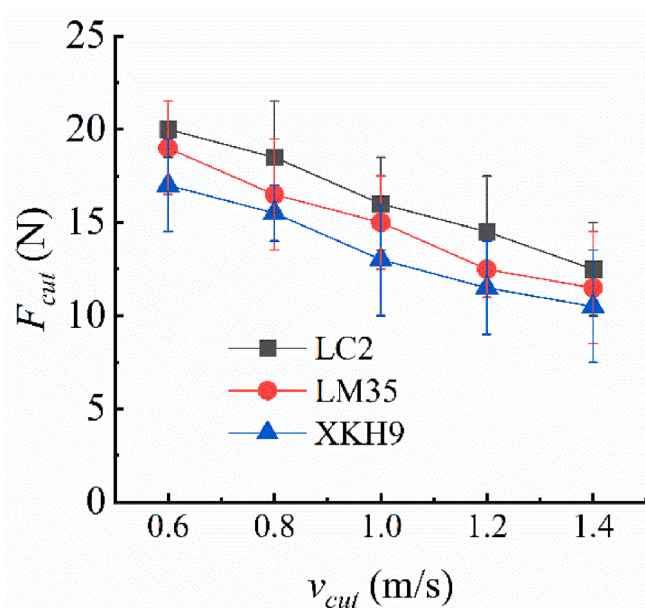


Fig. 18. Relationship between cutting force and cutting speed for three wheat varieties, showing mean values with standard deviation.

the value of the second cut, which can be explained by the established flexible model of wheat. The weight of the wheat spike was more concentrated and the stiffness of the stalks was small, so that it appeared ‘head-heavy’ in the simulations, resulting in the bending phenomenon of the wheat plant. This made the first cut with two stalks broken at the head of the knife and another two stalks broken at the end of the knife, leading to a relatively dispersed force in the knife-cutting process. Note that LM35 is selected as the example because it exhibits the largest error, whereas other two varieties show smaller errors. Thus, LM35 is taken as the representative case for detailed analysis. Generally, the analysis indicated that the wheat plant model established in the study can be used in the simulation of the cutting test for optimising the working conditions during the cutting process.

#### 4.3. Analysis of the threshing test and simulation results

Fig. 21 presents the simulations of the threshing process for wheat plants. At the early stage of threshing (Fig. 21a), the wheat plants entered the threshing area, the grains started to separate from the spike axis of the wheat ear due to the impact of the roller. In the middle stage of threshing (Fig. 21b), the spike axis of wheat ears and stalks were gradually deformed and broken by the continuous impact and kneading of the roller, resulting in a larger number of grains falling off from the wheat ears. At the end of threshing (Fig. 21c), the separated wheat grains were collected by the boxes below that were marked 1–5 for statistical analysis.

The total threshing rate obtained from the experiments and simulations was calculated for three wheat varieties as shown in Fig. 22. The results showed that the threshing rate for the experiments and

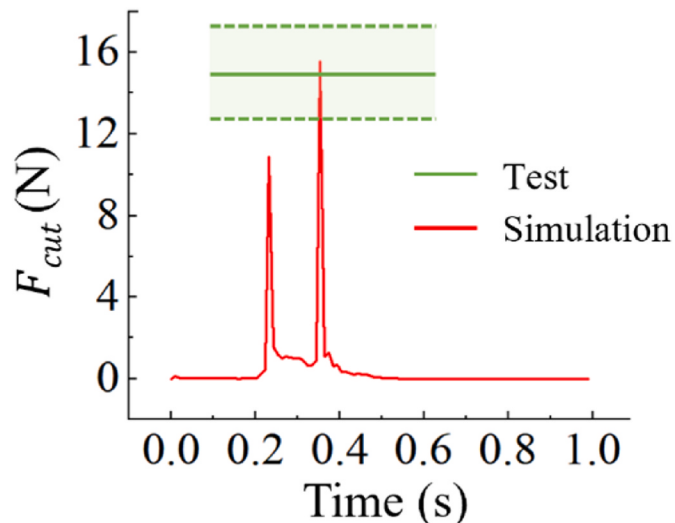


Fig. 20. Variation of cutting force in simulation for LM35. The cutting force obtained from the test is the maximum value during the stalk-cutting process. Here, a single test value is presented for the comparison.

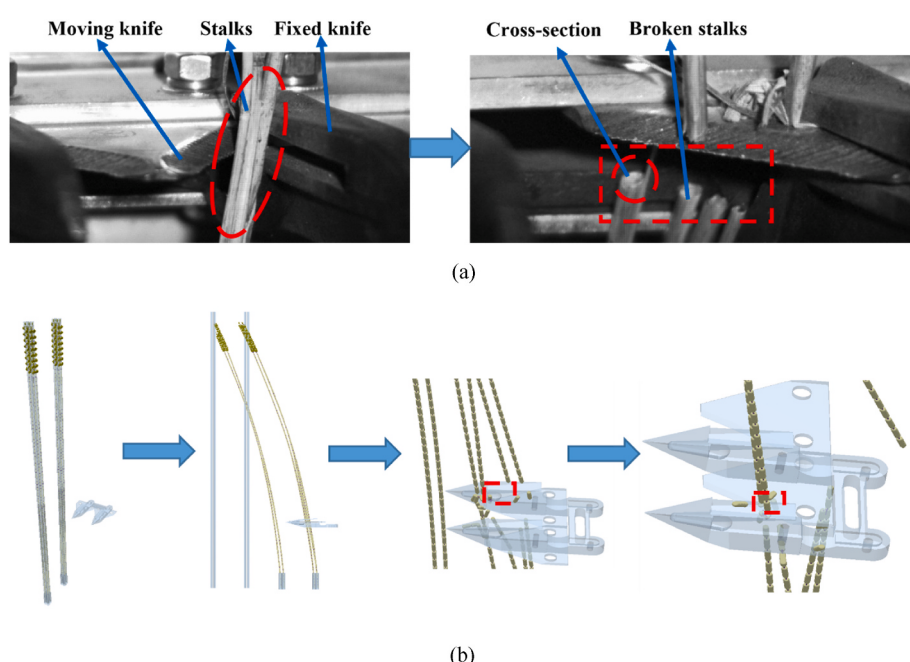
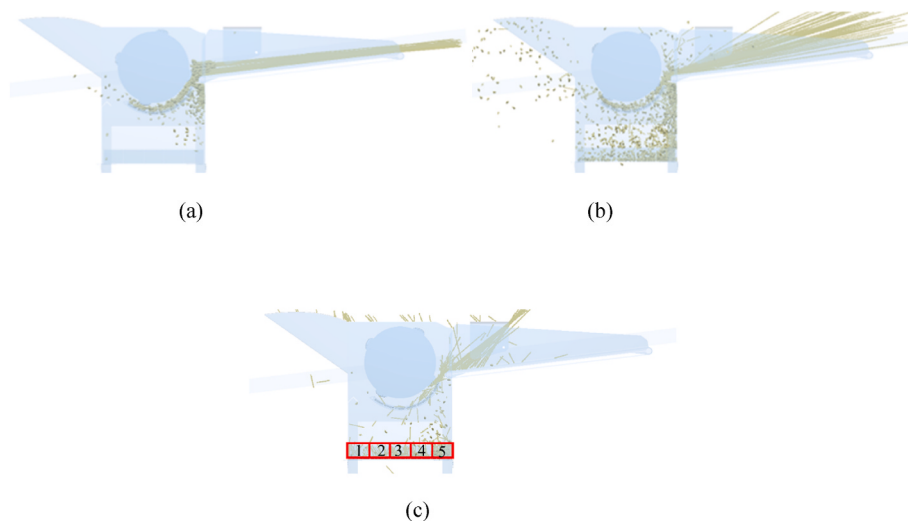
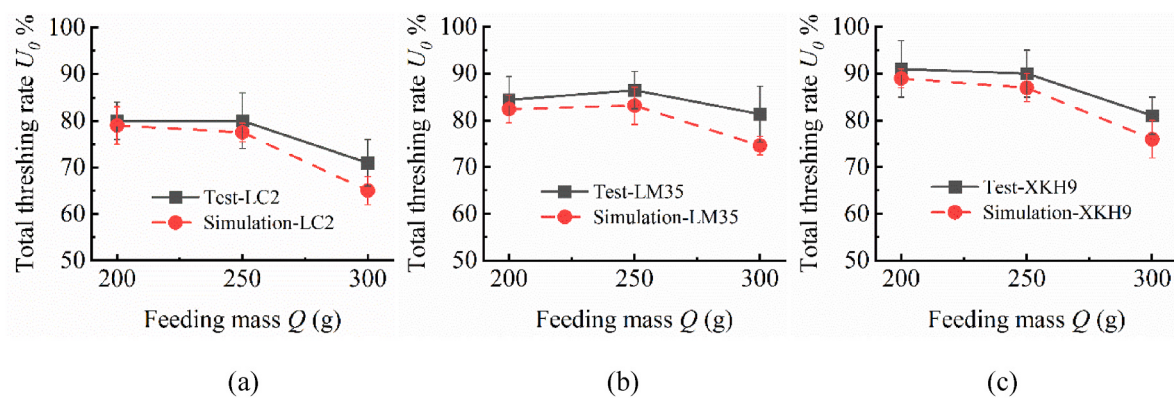


Fig. 19. Cutting process for LM35. (a) Cutting test process; (b) The simulation for cutting process.



**Fig. 21.** Threshing process of wheat plants at different stages: (a) early stage, plants are entered into the thresher and grains begin to detach; (b) mid-stage, the wheat ears experience the impact and friction, grains are separated from the ears; (c) end stage, the falling grains are collected by the box.



**Fig. 22.** Relationship between total threshing rate and feeding masses. (a) LC2; (b) LM35; (c) XKH9.

simulations did not change much with a change in the feeding mass (200–300 g). The total threshing rate obtained from the simulation is slightly lower than the experimental values. This discrepancy is due to plants in the simulation having identical parameters, whereas in the actual experiments, individual plants exhibit slight variations in shape and mechanical properties, causing the simulated wheat ears to experience more concentrated impacts, which makes the grains detach more

easily. The total threshing rate calculated from the simulation agreed well with the experiment results for LC2, LM35 and XKH9. Regarding the model accuracy, minimal error between the experiment and simulation results occurred when the feeding mass was 200 g. All the errors fell within a 9 % range, which verifies the proposed wheat plant model to be feasible and acceptable.

Detailed analysis of the distribution of grains and impurities (stalks

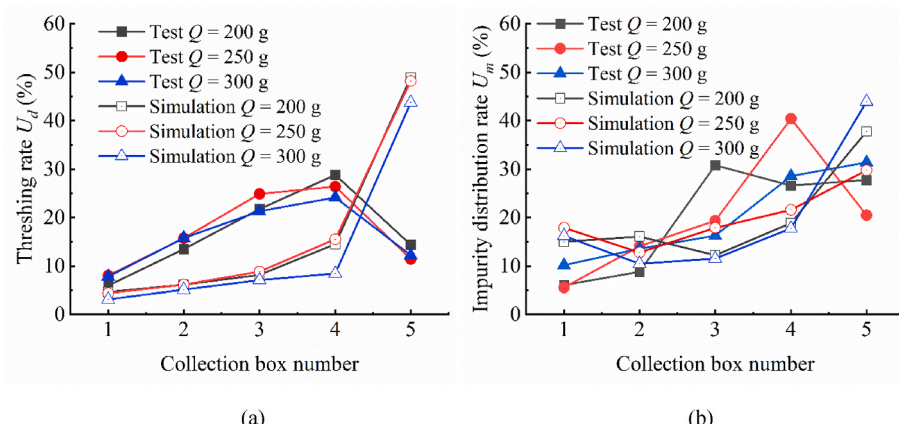


**Fig. 23.** Threshing results of the wheat plant for different feeding masses obtained from the actual tests and simulations. (a) Threshing rate of each collection box for different feeding masses; (b) Impurity distribution rate of each collection box for different feeding masses.

and spike axial segment) in each collection box at different feeding masses was performed. As can be seen in Fig. 23a, the threshing rate obtained from the simulations increased with the collection box number. The largest percentage of grain mass distribution was found in collection box No. 5, followed by collection boxes No. 4, No. 3, No. 2, and No. 1. The mass distribution of wheat grain exhibited differences with the results of the actual test for boxes No. 2, 3 and 4. In particular, there was an inverse tendency for the mass distribution in box No.5. Concerning the impurity distribution rate for each box, Fig. 23b shows that the impurity mass in the collection boxes from No. 1 to No. 5 gradually increased under different feeding masses. Though there was a discrepancy, the simulation results were aligned with the actual test in terms of the trend of impurity mass distribution.

Apart from the feeding mass, drum rotation speeds have an influence on the total threshing rate for the wheat plant. Fig. 24 shows that the total threshing rate increased gradually with the drum rotation speed for all three wheat varieties. The modelling results were supported by the trend of the experimental data. It can be seen that the maximum error between the simulation and experiment was within 5 % when the drum rotation speed was 666 rpm. As the drum rotation speed increased further to 888 rpm and 1100 rpm, the total threshing rate of the experiment was slightly larger than the simulation value, and the error was within 8 %. This was due to the fact that there was no protective effect of the glumes in the established wheat model, which were easily dislodged by the direct impact of the threaded rod of the drum at the early stage of threshing. The faster the drum speed, the more rapid the grains were brought to the exit under the impact of the threshing machine, which resulted in the grains in the collection box being slightly smaller than those in the actual test.

The distribution of grains and impurities in the individual collection boxes at different drum rotation speeds is shown in Fig. 25. The threshing rate of each box increased with box number 1–4 both for experiments and simulations (Fig. 25a). However, there was an opposite tendency for grain mass distribution in collection box No. 5, where the  $U_d$  continued to increase in the simulation but decreased in the experiment. Such a distribution led to a large error between the simulation and the actual test for the mass distribution in box No.5. Regarding the percentage of impurities, Fig. 25b shows that the mass proportion of impurities in the collection boxes gradually increased from No. 1 to No. 5 under different drum rotation speeds. It was found that the simulation results of the impurity mass distribution were consistent with the actual situation.

The error for grain threshing rate between the experiments and simulations was further analysed, particularly for the situation of each collection box. Firstly, in the actual test, the grains in the wheat ear were protected on both sides by the glumes, which slightly reduced the direct collision of external forces, slowing down the separation of the grains from the wheat ear. In the wheat plant model, the bonds between the grains and the wheat ears were easier to break, thus affecting the mass

distribution of the threshing material. In addition, the parameters of each plant were the same in the simulation. However, in the actual test, there were subtle differences in shape and mechanical properties among the plants, which led to the impact on the wheat ears in the simulation being more concentrated than in the actual situation, thus making the grains more likely to fall off. Since collection box No.5 was close to the entrance, a large number of the grains started to separate from the wheat ear once the wheat plants were transported into the drum in the simulations. This is the reason that the threshing rate in collection box No.5 was much higher than that of the experiment results. Secondly, the threshing drum rotation speed ranged from 666 rpm to 1100 rpm, corresponding to the linear speed ranging from  $9.76 \text{ m s}^{-1}$  to  $16.12 \text{ m s}^{-1}$ . It produced a large relative velocity between the plant model and the threaded rod at the early stage of the threshing, resulting in a significant dynamic impact effect. The mechanical parameters of the bonds in each part of the plant model were measured under quasi-static conditions. Therefore, the bonds were more likely to break in the dynamic impact situation, especially in the wheat ear, due to the small radius of the particles and bonds. The non-uniformity of geometry and mechanical properties of the wheat plant, and the bond breakage under dynamic impact loading, are identified as the primary source of error in the threshing rate. Despite these limitations, the total threshing rate obtained from simulations remains consistent with that in actual tests.

## 5. Conclusion

In this paper, a wheat plant model based on the discrete element method with continuous deformation and breakable characteristics is proposed to solve the problem of lacking generality and narrow scope of application. The wheat plant can be simplified into two parts a wheat ear (ear and grains) and a wheat stalk by analysing the geometry and size of three wheat varieties. Particle arrangement methods, combining geometric feature parameters, were employed to construct a flexible wheat plant model, which was determined by using the Hertz-Mindlin (no slip) contact and the bonding models in EDEM software. The flexible model not only effectively simulated the geometrical characteristics of wheat plants, but also accurately represented the flexibility and fracture behaviour. The feasibility and effectiveness of the modelling method was verified through the comparison of experiment and simulation results of the cutting and threshing processes. The simulation results were consistent with the experiment values in terms of the cutting force, threshing rate and impurity distribution rate, indicating that the geometric, contact and bonding parameters of the established model have high accuracy. The proposed general wheat plant model can more realistically reproduce the physical behaviour during the harvest process, providing an important reference for improving harvesting equipment and optimising the harvest process.

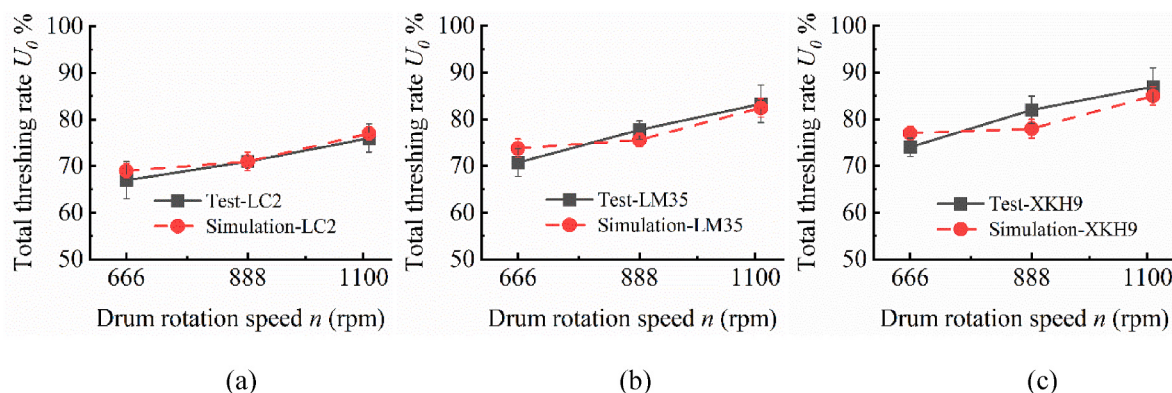
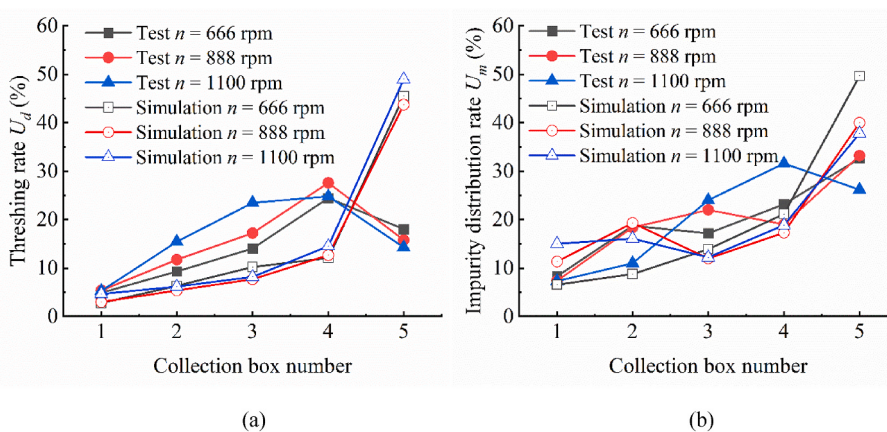


Fig. 24. Relationship between total threshing rate and drum rotation speeds. (a) LC2; (b) LM35; (c) XKH9.



**Fig. 25.** Threshing results of the wheat plant obtained at different drum rotation speeds. (a) Threshing rate of each collection box; (b) Distribution of impurity distribution rate of each collection box.

## CRediT authorship contribution statement

**Jianhua Fan:** Writing – review & editing, Writing – original draft, Validation, Methodology, Investigation, Formal analysis, Conceptualization. **Liang Zhang:** Writing – review & editing, Writing – original draft, Methodology, Investigation, Conceptualization. **Kai Sun:** Validation, Methodology. **Xiaoyan Qian:** Investigation. **Lu Wang:** Writing – review & editing, Writing – original draft, Supervision, Methodology, Investigation. **Jianqun Yu:** Methodology.

## Declaration of competing interest

The authors declare that they have no known competing financial interests or personal relationships that could have appeared to influence the work reported in this paper.

## Acknowledgements

This work was supported financially by the Department of Science and Technology of Jilin Province of China (Grant No. 20240303040NC), and the National Natural Science Foundation of China (No. 52130001).

## References

- Chen, X., He, X., Wang, W. Z., Qu, Z., & Liu, Y. (2022). Study on the technologies of loss reduction in wheat mechanization harvesting: A review. *Agriculture-Basel*, 12(11), 1935. <https://doi.org/10.3390/agriculture12111935>
- Dong, T., Yang, S. L., & Wang, S. (2024). Super-quadrupole DEM study of cylindrical particle behaviours in a rotating drum. *Powder Technology*, 437, Article 119511. <https://doi.org/10.1016/j.powtec.2024.119511>
- Fan, J., Wang, H., Sun, K., Zhang, L., Wang, L., Zhao, J., & Yu, J. (2024). Experimental verification and simulation analysis of a multi-sphere modelling approach for wheat seed particles based on the discrete element method. *Biosystems Engineering*, 245, 135–151. <https://doi.org/10.1016/j.biosystemseng.2024.07.009>
- Fei, J. M., Feng, W. Y., Shen, S. H., Han, Y. L., Li, A. Q., Hao, X. Z., ... Li, Z. Z. (2023). Non-uniform milling caused by preferential orientation of rice grains in friction rice mills. *Biosystems Engineering*, 235, 15–30. <https://doi.org/10.1016/j.biosystemseng.2023.09.011>
- Guo, Y., Wassgren, C., Hancock, B., Ketterhagen, W., & Curtiss, J. J. P. T. (2013). Validation and time step determination of discrete element modeling of flexible fibers. *Powder Technology*, 249, 386–395. <https://doi.org/10.1016/j.powtec.2013.09.007>
- He, P. F., Li, J., Zhang, D. Q., & Wan, S. (2018). Optimisation of the harvesting time of rice in moist and non-moist dispersed fields. *Biosystems Engineering*, 170, 12–23. <https://doi.org/10.1016/j.biosystemseng.2018.03.008>
- Horabik, J., & Molenda, M. (2016). Parameters and contact models for DEM simulations of agricultural granular materials: A review. *Biosystems Engineering*, 147, 206–225. <https://doi.org/10.1016/j.biosystemseng.2016.02.017>
- Horabik, J., Wiacek, J., Parafinikut, P., Banda, M., Kobylka, R., Stasiak, M., & Molenda, M. (2020). Calibration of discrete-element-method model parameters of bulk wheat for storage. *Biosystems Engineering*, 200, 298–314. <https://doi.org/10.1016/j.biosystemseng.2020.10.010>
- Ji, H., He, X., Ding, L., Qu, Z., Huang, W. K., & Wang, W. Z. (2022). Tobit model-based analysis on the influencing factors of wheat loss during harvesting by the combine harvester. *Journal of Computational Methods in Sciences and Engineering*, 22(2), 457–470. <https://doi.org/10.3233/JCM-215755>
- Ji, S., Wang, S., & Peng, Z. (2019). Influence of external pressure on granular flow in a cylindrical silo based on discrete element method. *Powder Technology*, 356, 702–714. <https://doi.org/10.1016/j.powtec.2019.08.083>
- Lenaerts, B., Aertsen, T., Tijskens, E., De Ketelaere, B., Ramon, H., De Baerdemaeker, J., & Saeks, W. (2014). Simulation of grain-straw separation by discrete element modeling with bendable straw particles. *Computers and Electronics in Agriculture*, 101, 24–33. <https://doi.org/10.1016/j.compag.2013.12.002>
- Li, H., Wang, J. S., Yuan, J. B., Yin, W. Q., Wang, Z. M., & Qian, Y. Z. (2017). Analysis of threshed rice mixture separation through vibration screen using discrete element method. *International Journal of Agricultural and Biological Engineering*, 10(6), 231–239. <https://doi.org/10.25165/j.ijabe.20171006.2910>
- Li, X. P., Zhang, W. T., Xu, S. D., Du, Z., Ma, Y. D., Ma, F. L., & Liu, J. (2023). Low-damage corn threshing technology and corn threshing devices: A review of recent developments. *Agriculture-Basel*, 13(5), 1006. <https://doi.org/10.3390/agriculture13051006>
- Liu, F. Y., Zhang, J., & Chen, J. (2018). Modeling of flexible wheat straw by discrete element method and its parameters calibration. *International Journal of Agricultural and Biological Engineering*, 11(3), 42–46. <https://doi.org/10.25165/j.ijabe.20181103.3381>
- Ma, Z., Han, M., Li, M. Y., Yu, C. S., & Chandio, F. A. (2020). Comparing kernel damage of different threshing components using high-speed cameras. *International Journal of Agricultural and Biological Engineering*, 13(6), 215–219. <https://doi.org/10.25165/j.ijabe.20201306.5395>
- Mao, H., Wang, Q., & Li, Q. (2020). Modelling and simulation of the straw-grain separation process based on a discrete element model with flexible hollow cylindrical bonds. *Computers and Electronics in Agriculture*, 170, Article 105229. <https://doi.org/10.1016/j.compag.2020.105229>
- Moya, M., Sánchez, D., & Villar-García, J. R. (2022). Values for the mechanical properties of wheat, maize and wood pellets for use in silo load calculations involving numerical methods. *Agronomy-Basel*, 12(6), 1261. <https://doi.org/10.3390/agronomy12061261>
- Potyondy, D. O., & Cundall, P. A. (2004). A bonded-particle model for rock. *International Journal of Rock Mechanics and Mining Sciences*, 41(8), 1329–1364. <https://doi.org/10.1016/j.ijrmms.2004.09.011>
- Schramm, M., & Tekeste, M. Z. (2022). Wheat straw direct shear simulation using discrete element method of fibrous bonded model. *Biosystems Engineering*, 213, 1–12. <https://doi.org/10.1016/j.biosystemseng.2021.10.010>
- Schramm, M., Tekeste, M. Z., Plouffe, C., & Harby, D. (2019). Estimating bond damping and bond Young's modulus for a flexible wheat straw discrete element method model. *Biosystems Engineering*, 186, 349–355. <https://doi.org/10.1016/j.biosystemseng.2019.08.003>
- Shi, Y. Y., Jiang, Y., Wang, X. C., Thuy, N. T. D., & Yu, H. M. (2023). A mechanical model of single wheat straw with failure characteristics based on discrete element method. *Biosystems Engineering*, 230, 1–15. <https://doi.org/10.1016/j.biosystemseng.2023.03.017>
- Sun, Z., Tang, H. W., Espinoza, D. N., Balhoff, M. T., & Killough, J. E. (2018). Discrete element modeling of grain crushing and implications on reservoir compaction. *Journal of Petroleum Science and Engineering*, 171, 431–439. <https://doi.org/10.1016/j.petrol.2018.07.046>
- Sun, K., Yu, J. Q., Liang, L. S., Wang, Y., Yan, D. X., Zhou, L., & Yu, Y. J. (2022). A DEM-based general modelling method and experimental verification for wheat seeds. *Powder Technology*, 401, Article 117353. <https://doi.org/10.1016/j.powtec.2022.117353>
- Sun, K., Yu, J. Q., Zhao, J. W., Liang, L. S., Wang, Y., & Yu, Y. J. (2023). A DEM-based general modeling method and experimental verification for wheat plants in the mature period. *Computers and Electronics in Agriculture*, 214, Article 108283. <https://doi.org/10.1016/j.compag.2023.108283>
- Wang, T., Yi, F. J., Wu, X. M., Liu, H. L., & Zhang, Y. Y. (2024). Calamitous weather, yield risk and mitigation effect of harvest mechanisation: Evidence from China's winter

- wheat. *The Australian Journal of Agricultural and Resource Economics*, 68(2), 386–412. <https://doi.org/10.1111/1467-8489.12545>
- Wang, S., Yu, Z. H., Zhang, W. J., & Aorige. (2022). Study on the modeling method of sunflower seed particles based on the discrete element method. *Computers and Electronics in Agriculture*, 198, Article 107012. <https://doi.org/10.1016/j.compag.2022.107012>
- Wang, L. J., Zhou, W. X., Ding, Z. J., Li, X. X., & Zhang, C. G. (2015). Experimental determination of parameter effects on the coefficient of restitution of differently shaped maize in three-dimensions. *Powder Technology*, 284, 187–194. <https://doi.org/10.1016/j.powtec.2015.06.042>
- Wang, S., Zhuravkov, M., & Ji, S. (2020). Granular flow of cylinder-like particles in a cylindrical hopper under external pressure based on DEM simulations. *Soft Matter*, 16(33), 7760–7777. <https://doi.org/10.1039/c9sm02435b>
- Zeng, Z., & Chen, Y. (2019). Simulation of straw movement by discrete element modelling of straw-sweep-soil interaction. *Biosystems Engineering*, 180, 25–35. <https://doi.org/10.1016/j.biosystemseng.2019.01.009>
- Zhang, Z., Liu, Y., Zheng, B., Li, R., & Sun, P. (2021). Discharge characteristics of binary particles in a rectangular hopper with inclined bottom. *Computational Particle Mechanics*, 8, 315–324. <https://doi.org/10.1007/s40571-020-00332-7>
- Zhao, S., Evans, T. M., & Zhou, X. (2018). Effects of curvature-related DEM contact model on the macro- and micro-mechanical behaviours of granular soils. *Géotechnique*, 68 (12), 1085–1098. <https://doi.org/10.1680/jgeot.17.P.158>
- Zhao, J., Yu, J., Sun, K., Wang, Y., Liang, L., Sun, Y., ... Yu, Y. (2024). A discrete element method model and experimental verification for wheat root systems. *Biosystems Engineering*, 244, 146–165. <https://doi.org/10.1016/j.biosystemseng.2024.06.004>
- Zhong, W. Q., Yu, A. B., Liu, X. J., Tong, Z. B., & Zhang, H. (2016). DEM/CFD-DEM modelling of non-spherical particulate systems: Theoretical developments and applications. *Powder Technology*, 302, 108–152. <https://doi.org/10.1016/j.powtec.2016.07.010>
- Zhou, L., Yu, J. Q., Liang, L. S., Yu, Y. J., Yan, D. X., Sun, K., & Wang, Y. (2021). Study on key issues in the modelling of maize seeds based on the multi-sphere method. *Powder Technology*, 394, 791–812. <https://doi.org/10.1016/j.powtec.2021.09.020>
- Zhou, L., Yu, J. Q., Wang, Y., Yan, D. X., & Yu, Y. J. (2020). A study on the modelling method of maize-seed particles based on the discrete element method. *Powder Technology*, 374, 353–376. <https://doi.org/10.1016/j.powtec.2020.07.051>